Optical response of ferromagnetic YTiO$_3$ studied by spectral ellipsometry

N.N. Kovaleva, A.V. Boris, P. Yordanov, A. Maljuk, E. Brüchner,
J. Strempfer, M. Konuma, I. Zegkinoglou, and B. Keimer

Max-Planck-Institut für Festkörperforschung, Heisenbergstrasse 1, D-70569 Stuttgart, Germany

C. Bernhard

Department of Physics, University of Fribourg, Chemin du Musée 3, CH-1700, Fribourg, Switzerland

A. M. Stoneham

*Department of Physics and Astronomy, University College London,
Gower Street, London WC1E 6BT, United Kingdom*

(Dated: February 5, 2008)

We have studied the temperature dependence of spectroscopic ellipsometry spectra of an electrically insulating, nearly stoichiometric YTiO$_3$ single crystal with ferromagnetic Curie temperature $T_C = 30$ K. The optical response exhibits a weak but noticeable anisotropy. Using a classical dispersion analysis, we identify three low-energy optical bands at 2.0, 2.9, and 3.7 eV. Although the optical conductivity spectra are only weakly temperature dependent below 300 K, we are able to distinguish high- and low-temperature regimes with a distinct crossover point around 100 K. The low-temperature regime in the optical response coincides with the temperature range in which significant deviations from Curie-Weiss mean field behavior are observed in the magnetization. Using an analysis based on a simple superexchange model, the spectral weight rearrangement can be attributed to intersite $d_i^1 d_j^1 \longrightarrow d_i^2 d_j^0$ optical transitions. In particular, Kramers-Kronig consistent changes in optical spectra around 2.9 eV can be associated with the high-spin-state ($^3T_1$) optical transition. This indicates that other mechanisms, such as weakly dipole-allowed $p-d$ transitions and/or exciton-polaron excitations, can contribute significantly to the optical band at 2 eV. The recorded optical spectral weight gain of 2.9 eV optical band is significantly suppressed and anisotropic, which we associate with complex $spin-orbit-lattice$ phenomena near ferromagnetic ordering temperature in YTiO$_3$.

I. INTRODUCTION

The relationship between the orbital state and the physical properties of YTiO$_3$, along with its antiferromagnetic partner LaTiO$_3$, has generated significant recent attention. Electronic structure calculations predict a specific, four-sublattice arrangement of t_{2g} orbitals supporting ferromagnetic order in YTiO$_3$ [1, 2, 3, 4, 5]. Direct evidence for an orbitally ordered state akin to that predicted in theoretical work has come from neutron diffraction [6]. X-ray absorption [7] and nuclear quadrupole resonance studies [8] have yielded supporting evidence. However, some major questions remain open. While electronic-structure calculations generically predict a strong spatial anisotropy of the superexchange parameters, inelastic neutron scattering experiments have revealed an almost isotropic spin wave spectrum [9]. The spectrum of orbital excitations recently revealed by Raman scattering is also in stark contrast to predictions based on the theoretically proposed orbitally ordered state [10]. Collective quantum zero-point fluctuations that strongly reduce the orbital order might offer a way out of this conundrum, but theoretical work on this scenario is still in its early stages [11].

Here we present a comprehensive ellipsometric study of the optical properties of stoichiometric YTiO$_3$, following the same methodology as in previous work on LaMnO$_3$ [12]. In LaMnO$_3$, the Mott-insulating progenitor of a family of compounds exhibiting colossal magnetoresistance, a realistic quantitative description of the interplay between spin and charge correlations has found possible [12]. The four d-electrons of LaMnO$_3$ are subject to a nearly cubic crystal field that splits the energy levels available to these electrons into a higher-lying, doubly degenerate e_g state and a lower-lying, triply degenerate t_{2g} state. Following Hund's rules, these states are occupied by one and three electrons, respectively, so that the e_g valence electron occupies a doubly degenerate level. This degeneracy is lifted by a cooperative Jahn-Teller distortion ("orbital order") around 800 K. The anisotropic charge distribution that goes along with orbital order gives rise to optical birefringence. In particular, the spectral weight of the Mott gap excitations around 2 eV becomes anisotropic below 800 K [13]. Ellipsometric measurements revealed that this anisotropy increases strongly below the antiferromagnetic ordering temperature of ~ 150 K [12]. The dependence of the optical spectra on the alignment of nearest-neighbor Mn spins reveals that the lowest-energy excitations are intersite $d-d$ transitions. A quantitative description of the tem-

perature dependence of the optical spectral weight could be achieved, based on the realization that the same fundamental mechanisms that determine the spectral weight of the optical excitations (namely, the Pauli principle and Hund's rules) also underlie the superexchange interaction parameters between Mn spins that had been obtained independently by inelastic neutron scattering.

As YTiO$_3$ is isostructural to LaMnO$_3$, but possesses only a single valence d-electron, it is not unreasonable to expect that its optical properties are amenable to a description in the same framework. However, there are several important differences between both compounds. YTiO$_3$ is *ferromagnetic* below $T_C \sim 30$ K [9] and it is hence an uncommon example of an electrically insulating ferromagnet. Moreover, YTiO$_3$ does not exhibit any structural phase transition below its chemical decomposition temperature of around 700 K [14]. A cooperative Jahn-Teller effect akin to that in LaMnO$_3$ is thus not apparent in its phase behavior. These differences are rooted in the microscopic properties of the orbitals occupied by the valence electrons. Specifically, the d-electron of YTiO$_3$ occupies the t_{2g} manifold, which exhibits a higher degeneracy and weaker lattice coupling than the e_g electron in LaMnO$_3$.

The comprehensive optical spectroscopy study of carefully prepared single crystals of YTiO$_3$ reported here was designed to motivate and guide further theoretical work on the interplay between spin and charge correlations in the titanates. The experiments proved surprisingly difficult, because the optical spectra were found to depend strongly on the type of surface exposed to the beam. Through extensive characterization measurements, this effect could be traced to an accumulation of oxygen defects near some (but not all) surfaces of the perovskite structure. Special care has to be taken in order to maintain stoichiometry in the crystal volume probed by the beam. After these difficulties were overcome, the results revealed a situation that is strikingly different from that in LaMnO$_3$. Notably, the optical spectrum depends only weakly on light polarization and on temperature, and the spectral weight rearrangement at the Curie temperature is extremely small. A noticeable spectral weight rearrangement is, however, observed at about 100 K, far above the Curie temperature. Possible origins of this effect are discussed.

II. CRYSTAL GROWTH AND CHARACTERIZATION

A. Crystal growth

Single crystals of YTiO$_3$ were grown by the floating zone method in a reducing atmosphere (Ar/H$_2$ = 50/50). The starting material was prepared by mixing appropriate amounts of Y$_2$O$_3$ (5N) and Ti$_2$O$_3$ (3N) powders in ethanol (99.8% purity). Note that commercially available Y$_2$O$_3$ powders contain 0.6 - 0.8 wt.% of water. Ignoring this during the feed rod preparation leads either to a deficiency of yttrium, or to titanium oxide impurities in the as-grown crystal. The mixture was calcined at $950°C$ in Al$_2$O$_3$ crucibles for 12h in vacuum (10^{-6} mbar). The calcined powder was formed into a cylindrical shape of 7-8 mm in diameter and 100 mm in length, and pressed at a hydrostatic pressure of about 400 MPa. The rods were sintered at 1050°C for 12 h under the same vacuum conditions. The apparatus used for crystal growth was a four-mirror-type infrared image furnace (Crystal System Corp., FZ-T-10000-H-III-VPR) equipped with four 1.5 kW halogen lamps. In the growth process the seed and feed shafts were rotated in opposite directions at rates of 10-15 rpm, the pulling rate was varied from 5 to 10 mm/h. The grown ingots were cut into wafers perpendicular to the growth direction, and both sides of wafers were polished to mirror finish. Then polished specimens were characterized using a polarizing optical microscope to examine the presence of sub-grains and inclusions.

B. Structure and oxygen stoichiometry

YTiO$_3$ exhibits the orthorhombic structure of GdFeO$_3$ type of *Pbnm* space group (see Fig. 1). X-ray diffraction measurements show that the YTiO$_3$ single crystals used for our experiments are untwinned, with mosaicity less than 0.03°. At room temperature, the lattice parameters are $a = 5.331(3)$, $b = 5.672(4)$, and $c = 7.602(6)$ Å, slightly different from those of Czochralski-grown single crystals reported by Maclean *et al.* [15]. The samples were aligned along the principal axes and cut in the form of a parallelepiped with dimensions $\sim 3 \times 3 \times 3$ mm^3.

The oxygen content was measured by heating small quantities of the as-grown crystals in O$_2$ flow using a DTA-TG apparatus. Due to the Ti$^{3+} \rightarrow$ Ti^{4+} instability, single crystals of YTiO$_3$ always have an excess of oxygen above the exact stoichiometry formula. Based on the weight gain, the oxygen excess in the formula YTiO$_{3+\delta}$ is estimated at a level less than $\delta = 0.013$ (see Fig. 2). As follows from the figure, Ti^{3+} ions fully oxidize to Ti^{4+} above 300 °C in flowing oxygen. It is important to mention that oxidation takes place above 450 °C in air. Therefore, one should avoid any warming above this temperature during the cutting and polishing procedures.

C. Magnetization

The samples were further characterized by magnetometry, using a superconducting quantum interference device. The inset of Fig. 3 shows temperature dependence of the magnetization for YTiO$_3$ sample in the vicinity of T_C taken on heating in a magnetic field of 1 kOe paral-

lel to the c-axis direction, after cooling in zero magnetic field. For the almost stoichiometric sample studied here, we estimate $T_C = 30$ K, amongst the highest values reported so far for YTiO$_3$.

In Fig. 3 we show the temperature dependence of the inverse susceptibility, $1/\chi_{mol}$, which exhibits a nearly linear increase above 100 K (χ_{mol} was corrected by a temperature-independent diamagnetic contribution χ_{dia} = - 5.7 × 10^{-5} emu/mol [8]). A fit to a Curie-Weiss law, $1/\chi_{mol} \approx \frac{8}{\mu_{eff}^2}(T - \theta)$, yields a Curie-Weiss temperature $\theta = 40$ K and an effective magnetic moment μ_{eff} = 1.66 μ_B, which is slightly reduced with respect to the spin-only value $\mu_S = 2\sqrt{S(S+1)} = 1.73\ \mu_B$ of the Ti^{3+} ions with S = 1/2. The magnetization data of Fig. 3 reveal significant deviations from Curie-Weiss mean-field behavior below about 100 K. As a result, an inflection point in the temperature-dependent magnetization is observed at 27 K, several degrees below T_C.

Figure 4 shows magnetization measurements for the three principal directions of YTiO$_3$ up to 7 T at 5 K, well below the magnetic transition temperature. These magnetic measurements reveal that the c-axis is the easy axis of magnetization, while the b-axis is hard. The saturated moment, which we estimate in the easy direction at the highest magnetic field of 7 T is $\mu^c = 0.84\ \mu_B$, whereas μ^b = 0.82 μ_B in the hard direction, both are reduced from one Bohr magneton. The data are in good agreement with those reported by Tsubota *et al.* [16] on single crystals also grown by a floating-zone method. By contrast, earlier data on single crystals grown by the Czochralski technique showed markedly reduced magnetic fields at which the saturation behavior of the magnetization sets on [17]. The anisotropy of the magnetization is also different: in the Czochralski-grown crystals, both the a- and c-axes were established to be easy axes.

III. RESULTS AND DISCUSSION

A. Technical details

For optical measurements the surfaces were polished to optical grade. The measurements in the frequency range of 4000-44000 cm^{-1} (0.5-5.5 eV) were performed with a home-built ellipsometer of rotating-analyzer type [18], where the angle of incidence is 70.0°. The sample was mounted on the cold finger of a helium flow UHV cryostat with a base pressure of 5x10^{-9} Torr at room temperature. In the spectral range 80-6000 cm^{-1} (0.01-0.75 eV) we used home-built ellipsometers in combination with a fast-Fourier transform interferometer at the infrared beam line of the ANKA synchrotron at the Forschungszentrum Karlsruhe, Germany [19]. In addition, near-normal incident reflectivity was measured in the phonon frequency range of 80-700 cm^{-1} using a Fourier transform spec-

trometer Bruker IFS66vs.

B. Infrared-active phonons

We now present a full set of spectra of infrared-active optical phonons. YTiO$_3$ has an orthorhombic crystal structure (space group *Pbnm*, D$_{2h}^{16}$) with four formula units per unit cell (see Fig. 1). A factor-group analysis yields a total number of 60 Γ-point phonons, of which 24 [7A$_g$+5B$_{1g}$+7B$_{2g}$+5B$_{3g}$] are Raman-active modes, 25 [9B$_{1u}$+7B$_{2u}$+9B$_{3u}$] are infrared-active modes, 8 A$_u$ are silent modes, and 3[B$_{1u}$+B$_{2u}$+B$_{3u}$] are acoustic modes. We performed spectroscopic ellipsometry on the ac- and bc-surfaces for all high-symmetry orientations of the optical axis with respect to the plane of incidence of light and near-normal incidence reflectivity measurements for **E** || **a**, **E** || **b**, and **E** || **c**.

In Fig. 5 we show low-temperature optical conductivity spectra in the phonon frequency range. The spectra were deduced from polarized reflectivity spectra via a standard Kramers-Kronig analysis, combined with the respective ellipsometry spectra for correct normalization. Our polarized optical measurements allowed us to observe fully anisotropic phonon spectra in YTiO$_3$ single crystals and make an assignment of the infrared-active modes according to their symmetry. For **E** || **a** we distinguish 9B$_{1u}$ normal modes at the frequencies 154, 210, 316, 336, 428, 440, 516, 554, and 577 cm^{-1}, for **E** || **b** we distinguish 9B$_{3u}$ normal modes at the frequencies 139, 240, 273, 309, 364, 380, 463, 523, and 578 cm^{-1}, and for **E** || **c** we distinguish 7B$_{2u}$ normal modes at the frequencies 165, 203, 322, 349, 386, 543, and 563 cm^{-1}. Our observation of fully polarized phonon spectra and its consistency with the symmetry analysis indicate good alignment of the crystal with respect to the crystallographic directions. Further, the narrow and intense phonon peaks are testimony to the excellent quality of our YTiO$_3$ crystal.

C. Surface defect states

We have found out that polarized optical spectra in YTiO$_3$ exhibit specific features associated with the surface type exposed to the beam. Figure 6 shows spectra of high-frequency, oxygen-dominated optical phonons measured with light polarized along the b-axis on different types of the surface associated with the ab and bc crystallographic planes. Although the main features are observed at the same frequencies in both cases, a number of side-band modes are present in measurements on the ab surface. A similar set of extra modes is observed in a-axis polarized measurements on the ab surface, compared to the ac surface. As single crystals of YTiO$_{3+\delta}$ easily accommodate extra oxygen, the appearance of the

weaker satellites in the phonon spectra can be naturally explained as arising from the coupling with local oxygen modes, associated with oxygen interstitials, predominating in the ab surface.

In addition, we show that the optical conductivity spectra close to the absorption edge are also dependent on the type of surface. In the inset of Fig. 7 one can see that the optical conductivity spectrum measured along the b-axis on the ab surface exhibits an optical band at about 0.8 eV, near the fundamental absorption edge. As a result, the absorption edge shifts to lower energies, compared to the bc surface. This may be an indication on the filling of the gap states with the energy levels associated with the defects predominating in the ab crystallographic plane. It is well known that the absorption within the optical gap in the RTiO$_3$ system is extremely sensitive to the oxygen stoichiometry [20, 21]. Therefore, these data provide additional evidence for the presence of defects associated with oxygen interstitials in the ab surface, in agreement with the phonon spectra.

Motivated by the optical data, we have performed surface-characterization measurements using Auger-electron spectroscopy (AES). Figure 8 shows typical AES sputter-depth profiles obtained by Ar$^+$ bombardment of different YTiO$_3$ surfaces. One can see that the titanium concentration is almost flat in the sputter-depth profile, and independent of the type of surface studied. This is also the case for the oxygen profile measured on the bc surface of YTiO$_3$ crystals. On the contrary, monitoring the oxygen concentration in the ab surface shows the profile significantly extended into the sample depth.

We now discuss the origin of the differences in oxygen defect concentration near the different types of surfaces. Ignoring the orthorhombic distortion for simplicity, we note that the bc- and ab-surfaces correspond (110) and (001) planes of the simple cubic perovskite structure, respectively (see Fig. 1). The atomic stacking sequences of these planes are O$_2$-YTiO-O$_2$-YTiO-... and YO-TiO$_2$-YO-TiO$_2$-..., so that the valence states of the constituent ions imply that these surfaces are polar. Polar surfaces are intrinsically unstable due to the macroscopic polarization caused by a dipole moment perpendicular to the surface generated by the alternating, oppositely charged planes [22]. For the perovskite structure of LaMnO$_3$, it has been shown by ab-$initio$ calculations [23] that the polarity can be lifted in different ways for different types of surfaces. For instance, a redistribution of charge is able to cancel the macroscopic polarization near the (001) surface, whereas surface oxygen vacancies serve as a better stabilizing factor at the (110) surface. Of course, these calculations cannot be simply transposed to YTiO$_3$, nonetheless, they indicate a possible microscopic origin of the differences in oxygen profiles and optical spectra revealed by our data.

Thus in the case of the ab surface (associated with the (001) plane of the perovskite structure) the charge redis-

tribution could result in a formation of the defects comprising oxygen interstitials in the extended near-surface region. This could effect the infrared oxygen phonon modes and optical absorption edge in YTiO$_3$ crystal, in agreement with our observations. Contrary to the ab surface, the perpendicular surfaces (associated with the (110) plane of the perovskite structure) could have predominantly surface defects. Accordingly, we clearly see that the optical conductivity spectra measured on the surfaces including the c-axis show a dip at around 4.5 eV, as illustrated by Fig. 7. This effect is by far more pronounced in the optical conductivity spectra and appears at the UV frequencies, close to the onset of the strongly dipole-allowed $p - d$ transition. These observations show the importance of the surface effects, associated with screening of the surface charges by crystal defects and bond-bending phenomena at the surface, on the optical conductivity of YTiO$_3$. Therefore, one should refer the polarized optical conductivity spectra to the type of the surface measured. Most of the measurements discussed below were taken on the bc-surface, where no excess oxygen is detected.

Aging effects on the optical spectra of samples kept in air for extended periods of time are presumably also related to oxygen incorporation. Nonequilibrium conditions at the crystal surface due to the Ti^{3+} $\rightarrow$ Ti^{4+} instability in air are conducive to the formation of the titanium oxides, with the valency of Ti increased above 3+, and simultaneous incorporation of extra oxygen (interstitials). Due to the diffusion processes these defects migrate from the surface into the crystal bulk and form an extended profile. In Fig. 7, optical conductivity spectra in b-axis polarization on freshly polished ab-surfaces are compared to identical data taken after about 1-1/2 years. The flat background, which sets on around 1.9 eV and extends to higher energies, decreases progressively with time. We show later on that the temperature evolution of the optical response measured on aged surfaces differs drastically from the temperature effects we associate with the bulk properties of stoichiometric YTiO$_3$.

D. Dielectric response and optical conductivity

1. Overall description and dispersion analysis

Figures 9 and 10 show the anisotropic real and imaginary parts of the dielectric function, $\tilde{\epsilon}(\nu) = \epsilon_1(\nu) + i\epsilon_2(\nu)$, and the optical conductivity $\sigma_1(\nu) = 1/(4\pi)\nu\epsilon_2(\nu)$ at T = 300 K extracted from ellipsometric data. In contrast to prior data deduced from reflectivity measurements via Kramers-Kronig analysis [20, 21, 24, 25] we are able to resolve a noticeable anisotropy in the intensity of the ab-plane and c-axis dielectric response. We can also distinguish a weak anisotropy within the ab-plane. In agreement with prior work [20, 21, 24, 25],

TABLE I: Parameters of Lorenz oscillators resulting from dispersion analysis of complex dielectric response in b-axis (c-axis) polarization in $YTiO_3$ measured on ab plane (bc plane) at T = 300 K, $\epsilon_\infty = 1.78$ ($\epsilon_\infty = 2.18$).

ν_j (eV)	S_j	γ_j (eV)	N_{eff}
1.95 (2.11)	1.25 (0.67)	1.68	0.21 (0.13)
2.94 (2.78)	0.20 (0.08)	1.46	0.07 (0.03)
3.72 (3.43)	0.08 (0.12)	0.96	0.05 (0.06)
5.05 (5.25)	0.22 (0.24)	0.80	0.24 (0.29)
5.61 (5.78)	0.84 (0.82)	1.15	1.14 (1.20)

our optical conductivity spectra exhibit a smooth onset of optical absorption around 0.5 eV (Fig. 7). Due to the Mott nature of the optical gap in $YTiO_3$, formed between the lower and upper d bands, the fundamental absorption edge is supposed to exhibit $d-d$ character. However, the origin of the low-energy transitions in optical spectra of $YTiO_3$ has not been addressed in details so far. In our $\epsilon_2(\nu)$ and $\sigma_1(\nu)$ spectra one can clearly see a lowest-energy optical band peaking around 1.9 eV, whereas the following optical transitions are strongly superimposed, and the optical spectra look like featureless background for the highly intense band around 5.5 eV. To separate contributions from the different low-energy optical bands, we perform a classical dispersion analysis. Figure 11 summarizes results of a dispersion analysis of the complex dielectric response for b-axis polarization measured on ab plane at T = 300 K. Using a dielectric function of the form $\tilde{\epsilon}(\nu) = \epsilon_\infty + \sum_j \frac{S_j}{\nu_j^2 - \nu^2 - i\nu\gamma_j}$, where ν_j, γ_j, and S_j are the peak energy, width, and dimensionless oscillator strength of the jth oscillator, and ϵ_∞ is the core contribution from the dielectric function, we fit a set of Lorenzian oscillators simultaneously to $\epsilon_1(\nu)$ and $\epsilon_2(\nu)$. In our analysis we introduce a minimum set of oscillators, with one oscillator beyond the spectral range investigated. The determined parameters of ν_j, S_j, and γ_j are listed in Table 1. In accordance with our dispersion analysis, the three low-energy optical bands are located at 2.0, 2.9, and 3.7 eV in b-axis polarization at T = 300 K. An important value is the associated spectral weight (SW), which can be estimated for the separate Lorentz oscillator as $SW = \int \sigma_1(\nu')d\nu' = \frac{\pi}{120}S_j\nu_j^2$. In Table 1 we list normalized SW values in terms of the effective numbers of electronic charge carriers $N_{eff} = \frac{2m}{\pi e^2 N}SW$, where m is the free electron mass and $N = a_0^{-3} = 1.7 \times 10^{22}$ cm^{-3} is the density of Ti atoms. Note that the dip in the optical c-axis response above 4 eV is strongly influenced by surface effects, as discussed in Section III.C above, therefore, the fit is less accurate in c-axis polarization. However, we have estimated the corresponding ν_j and S_j values in c-axis polarization, while keeping the widths of the optical bands, γ_j, the same as in b-axis polarization. These values are listed in Table I in round brackets.

Three main contributions have to be distinguished in the spectral range of interest here: (i) $p-d$ transitions from the occupied O $2p$-band into the partially occupied Ti d-levels; (ii) intra-site crystal-field (CF) $d-d$ transitions from the partially occupied Ti t_{2g} manifold into the empty e_g levels; and (iii) inter-site $d-d$ transitions within the t_{2g} manifold and between the t_{2g} and e_g levels. In addition, the associated excitonic and polaronic optical bands may also contribute in the spectral range of interest. Based on comparison to optical data on other transition metal oxides and to a variety of theoretical calculations [26, 27, 28], the pronounced optical band at $\sim$ 5.5 eV can be assigned to strongly dipole-allowed $p-d$ transition. An assignment of the lower-energy bands is, however, much more difficult. In particular, cluster calculations have identified a series of weakly dipole-allowed charge-transfer (CT) transitions $O2p \longrightarrow$ Ti $3d$ with energies and spectral weights comparable to those observed in our experiment [29]. These transitions overlap the $d-d$ transitions also expected to be present in this energy range.

2. Temperature dependence

Recent work on $LaMnO_3$ has shown that the temperature dependence of the optical spectral weight can be instrumental in tracking down the origin of the various features in the optical response [12]. The spectral weight of the inter-site $d-d$ transitions is very sensitive to the temperature dependent spin correlations, because the spin alignment controls the transfer of electrons between neighboring sites via the Pauli principle. The contribution from these transitions can thus be singled out by monitoring the evolution of the optical response through the onset of magnetic order, as demonstrated in $LaMnO_3$ [12].

Figure 12 shows that the temperature effect on the optical spectra is weak in the temperature range from room temperature down to low temperatures. The main effects are a shift of the absorption edge to higher energies and a narrowing of the strong optical band at about 5.5 eV. Our ellipsometric measurements also allowed us to resolve much weaker effects at low temperature, which one may associate with redistribution of optical spectral weight around the spin ordering temperature $T_C = 30$ K. Figures 13a and b show difference in the dielectric function spectra, $\Delta\epsilon_1(\nu)$ and $\Delta\epsilon_2(\nu)$, between 15 and 55 K, measured along the b- and c-axis, respectively. The b-axis difference spectra exhibit a weak resonance feature in $\Delta\epsilon_2(\nu)$ around 2.85 eV and an antiresonance feature (zero-crossing) in $\Delta\epsilon_1(\nu)$ at the same energy. The observed changes in $\tilde{\epsilon}(\nu)$ provide experimental evidence for the presence of an optical band centered around 2.85 eV. The intensity of this band increases below the Curie temperature. Similar reasoning shows that the intensity of the optical band around 3.95 eV decreases below T_C.

By contrast, the optical response in c-axis polarization is temperature independent in this spectral range, to within our experimental accuracy (Fig. 13b). Conversely, the increase in the intensity of the optical band around 1.8 eV observed in the c-axis difference spectra upon cooling below T_C has no obvious counterpart in the corresponding b-axis spectra. Finally, the optical response modification at the lowest energies, which is attributable to the shift of the absorption edge below T_C, is again most pronounced in b-axis polarization. This shift is much less pronounced than the high-temperature changes shown in the left panel of Fig. 12, but its direction is opposite.

Figure 14 shows the temperature dependence of the ϵ_2 amplitudes at the main peak positions, 1.8 and 2.85 eV, in b-axis polarization. In Fig. 15, ϵ_1 and ϵ_2 of the 1.8 eV peak, measured in c-axis polarization slightly off-resonance, are plotted as a function of temperature. Two temperature regimes can be distinguished. The temperature evolution at high temperatures is presumably mainly the result of lattice anharmonicity, which leads to a broadening and shift of spectral features with increasing temperature. Remarkably, a crossover then occurs at ~ 100 K, far above T_C. Below the crossover point, the temperature dependence of the SW at both peak positions changes sign. (Note that in b-axis polarization, the ϵ_2 amplitude of the 1.8 peak exhibits nonmonotonic and more complicated behavior, mainly due to the shift of the absorption edge to lower energies.) Within our experimental accuracy we are not able to resolve any anomaly at T_C. It is noteworthy that the crossover temperature in the optical spectra roughly coincides (within the experimental error) with the onset of deviation of the inverse susceptibility from the Curie-Weiss behavior discussed in Section II.C.

Figure 16 shows the associated spectral weight changes, $\Delta N_{eff}(15$ K, 55 K), in b- and c-axis polarizations, where we also plot b-axis $N_{eff}(\nu)$ spectrum at 15 K, where $N_{eff}(\nu) = \frac{2m}{\pi e^2 N} \int_{\nu_0}^{\nu} \sigma_1(\nu') d\nu'$. One can notice that b-axis spectral weight increases below T_C: (i) at low energies below 1.5 eV, due to the shift of the absorption edge, and (ii) in the spectral range from 2.2 to 3.5 eV, where it can be associated with a total spectral weight gain of the optical band at ~ 2.85 eV. In both cases (i) and (ii), one can estimate the SW gain due to FM ordering, $\Delta N_{eff}(15$ K, 55 K), by approximately the same amount of ~ 0.001. At higher energies, we relate the spectral weight decrease in the spectral range from 3.5 to 4.4 eV to the optical band around 3.95 eV, however, it is only weakly displayed. C-axis spectral weight changes primarily in the spectral range from 1.5 to 2.3 eV, where it can be associated with a total spectral weight gain of the optical band around ~ 1.8 eV. One can notice that, in the overall, the spectral weight changes in b-axis are much more pronounced than those in c-axis.

Based on our observations, we now discuss the origin of the optical transitions in YTiO$_3$. As discussed in Section III.D.2 above, the temperature dependence of the SW allows us to single out the contribution from intersite $d_i^1 d_j^1 \longrightarrow d_i^2 d_j^0$ charge excitations to the optical response. Such transitions lead to four different excited states: a high-spin (HS) $^3T_1$ state at energy $U^* - 3J_H$, two degenerate low-spin (LS) states $^1T_2$ and ^1E at energy $U^* - J_H$, and a LS state $^1A_1$ at energy $U^* + 2J_H$ [11, 30]. Here U^* is the effective Coulomb repulsion of the two electrons with opposite spins on the same t_{2g} orbital, and J_H is the Hund interaction. An ellipsometry study of the LaTiO$_3$ single crystal (characterized in [31]) has revealed that all optical bands are shifted to lower energies by ~ 0.5 eV compared to YTiO$_3$, presumably due to the screening effects. Based on this observation and the estimated value of the effective on-site electron correlation energy $U_{dd} \sim 4$ eV in LaTiO$_3$ [32], we estimate $U^* \sim 4.5$ eV in YTiO$_3$. The Hund's coupling constant is expected to be in the range 0.5–1 eV. (Note that the free-ion value is 0.59 eV [33]). The optical transition around 2.85 eV ($\pm$ 0.1 eV), which exhibits a SW increase in ab polarization at low temperatures, is therefore naturally assigned to a HS ($^3T_1$) transition, where the valence electron is transferred to an unoccupied t_{2g} orbital on the neighboring Ti site with a parallel spin. As the data are noisier at higher energies, the assignment of the band at 3.95 eV ($\pm$ 0.1 eV) is more difficult. With this caveat, it can be reasonably attributed to the lowest-lying LS transition, based on the observation of a SW decrease upon FM spin ordering. With the resulting tentative values of $U^* = 4.5 \pm 0.2$ eV and $J_H = 0.55$ eV $\pm$ 0.1 eV, the next LS transition is expected at ~ 5.6 eV, at the high-energy limit of our optical measurements. In our earlier optical study of LaMnO$_3$ we identified a HS state of $^6A_1$ symmetry at the energy $U^* - 3J_H + \Delta_{JT} \sim 2.0$ eV, where Δ_{JT} is the Jahn-Teller splitting energy of the e_g levels [12]. The estimated parameters $U^* \sim 2.8$ eV, $J_H \sim 0.5$ eV, and $\Delta_{JT} \sim 0.7$ eV yielded a good description of the observed spectra. This suggests a lower value of energy for the HS state multiplet in LaMnO$_3$ than in YTiO$_3$. As the values of U (and J_H) are supposed to follow certain semiempirical rules and are lower for early transition metal ions than for Mn or ions with almost filled $3d$ shells [34, 35], there is a controversy regarding the estimated U values in YTiO$_3$ and LaMnO$_3$. However, there is a good agreement between the U values estimated for the Ti oxides from photoemission spectra [36], t_{2g} resonant soft x-ray emission spectroscopy (SXES) [32], $ab-initio$ predictions [37], and from the present optical study. From this follows that environmental factors (covalency, polarisation, etc.), which are important in many oxide systems [38], are essential to the understanding the electronic correlations in LaMnO$_3$, in particular, optical transitions and electronic photoinization spectra [39].

This assignment suggests that the optical band at energy 2 eV (Figs. 9-12) is dominated by transitions of

different origins. One can see a noticeable shift of the absorption edge to higher energies with decreasing temperature in the left panel of Fig. 12. Theories of band-tail absorption ascribe this behavior to electrons interacting with a spatially random potential due to thermal and structural disorder [40]. Interestingly, the absorption edge shifts in the opposite direction below about 100 K, which results in a SW gain below 1.5 eV (see Fig. 13 (a) and Fig. 16). It is possible that this effect could be associated with spin-polaronic (or exciton-polaronic) states in the band-tail density of states or with contributions from indirect $d-d$ optical transitions. In addition, as we have discussed above, weakly dipole-allowed $p-d$ transitions [29] and intra-site (CF) $d-d$ transitions can contribute here. Further experimental and theoretical studies are required to estimate different contributions to the optical band at energy 2 eV.

We now focus on the absolute SW gain of the (HS) $^3T_1$-state $d-d$ transition centered around 2.85 eV due to *spin ordering* - between the high-temperature limit (HT) - disordered spins - and the low-temperature limit (LT) - FM ordered spins, as well as the SW gain at low temperatures. Via the optical sum rule in the tight-binding approximation, one finds $N_{eff} = (ma_0^2/\hbar^2)K$, where K is the kinetic energy associated with virtual charge excitations. The contribution of the (HS)$^3T_1$ excitation to the kinetic energy K can be estimated from a related term in the superexchange energy, $K = -2\langle H_{SE}(^3T_1)\rangle$. For the bond along the $\delta(= a, b, c)$ direction, $H_1^{(\delta)} = \frac{2t^2}{U-3J_H}(\bar{S}_i \cdot \bar{S}_j + 3/4)(A_{ij}^{(\delta)} - \frac{1}{2}n_{ij}^{(\delta)})$, where the orbital operators $A_{ij}^{(\delta)}, n_{ij}^{(\delta)}$ depend on the direction of the $\langle ij \rangle$ bond and t is the electron transfer amplitude [11, 30]. Provided the optical excitation energy of the HS-state at $U - 3J_H$ is specified, the optical spectral weight depends on the transfer amplitude t and the underlying orbital state. We estimate the SW in the framework of the isotropic F-type classical orbital ordering, considered by Oleś *et al.* [30]. The kinetic energy of the HS-state at $T = 0$ K is then expressed as $K_1^{(\delta)} = \frac{2}{3}\frac{4t^2}{U-3J_H}$. At high temperatures, spin disorder reduces this value by a factor of $1/4$. In the FM state the isotropic exchange constants are determined by $J_{FM}^{(\delta)} = -\frac{2}{3}\frac{4t^2 J_H}{(U-3J_H)(U-J_H)}$. Using the experimental value of the exchange constant $J^{(\delta)} = -3$ meV [9], and conservatively considering a wide range of Hund coupling constants 0.5 eV $\leqslant J_H \leqslant$ 1 eV, the transfer amplitude is estimated in the range 120 meV $\lesssim t \lesssim$ 160 meV, in reasonable agreement with *ab-initio* calculations [2]. The resulting estimate of the SW in the paramagnetic state, $0.022 \lesssim N_1^{(\delta)}(T \gg T_C) \lesssim 0.034$, is a factor of 2-3 lower than the b-axis experimental value listed in Table I. This estimate gives credence to our contention that inter-site $d-d$ transitions contribute substantially to the optical SW in this energy range. The same analysis yields a theoretical value of $0.008 \lesssim \Delta N_1^{(\delta)}$ (LT, HT) $\lesssim 0.012$ for the

SW gain of the (HS)$^3T_1$ transition due to *spin ordering*. The experimental value in b-polarization is ΔN_{HS}^{ab}(15K, 55K) $\simeq 0.002$, due to a total contribution from the direct $d-d$ transitions at ~ 2.85 eV and the indirect $d-d$ transitions (or spin-polaronic states) at the absorption edge (see Fig. 16). As the onset of the SW transfer is about 100 K, and the transfer is only about half complete at 55K, the difference between experimental and theoretical values is again about a factor of 2-3.

The absence of any noticeable temperature-dependent SW change of the band at 2.85 eV along the c-axis (Fig. 13b) disagrees with the simple analysis presented above. One might be tempted to attribute this discrepancy to a strong anisotropy of the superexchange parameters predicted by various theoretical calculations [1, 2]. However, according to our optical data, the spectral weight of the low-energy optical bands along the c-axis is only a factor of 1.5-2 smaller than in the ab-plane (Table I). Moreover, a direct determination of the exchange parameters by inelastic neutron scattering is inconsistent with this prediction [9].

To summarize the discussion, we note that the overall magnitude of the SW of the optical band at 2.85 eV and its temperature dependence in ab-polarization are in reasonable agreement with the predictions of a simple superexchange model, in analogy to LaMnO$_3$. However, the model overestimates the SW gain of the (HS)$^3T_1$ transition due to *spin ordering* by a factor of 2-3. In addition, the anisotropic temperature dependence of the optical SW indicates that an understanding of the optical conductivity of YTiO$_3$ requires mechanisms that go qualitatively beyond this simple model. These observations can be naturally understood as a consequence of a possible Ti t_{2g} orbital rearrangement between 55 K and 15 K. Then, the lowering of the optical spectral weight and the anisotropy come through selection rules of the modified ground state wavefunction.

This may imply an important *qualitative* difference between LaMnO$_3$ and YTiO$_3$. Almost undistorted TiO$_6$ octahedra in YTiO$_3$ indicate a small Jahn-Teller instability, resulting from the weak coupling between the two nearly-degenerate electronic ground states. The Jahn-Teller instability may disappear if there is sufficiently large splitting of the nearly-degenerate levels by some perturbation, in particular by the spin-orbit interactions [41, 42]. The orbital degrees of freedom may be essentially quenched in the magnetically ordered state, when the ground multiplet experiences splitting into two doublets, with concomitantly, a partial uncoupling of the spin and orbital moments. Then the temperature behavior in such a system is largely determined by the interplay between the spin-orbit coupling and the Jahn-Teller effect. In addition, the joint spin-and-orbital fluctuations, which develop at finite temperatures, can contribute significantly at $T > T_C$ [43]. In such a case, the establishment of the spin-spin correlations in ap-

proaching the magnetic transition will give rise to complex $spin-orbit-lattice$ effects, peculiar to the systems with orbital degrees of freedom. By contrast, the orbital degrees of freedom are quenched in $LaMnO_3$ by a large static Jahn-Teller distortion, and with the use of the same approach we have shown that the redistribution of the optical spectral weight is in a good agreement with a superexchange model that attributes these shifts to the temperature dependent correlations between Mn spins [12].

Finally, in Fig. 17 we show temperature dependence of the b-axis optical conductivity investigated on the aged surface of our $YTiO_3$ single crystal. In contrast to the temperature dependencies measured on freshly polished surfaces (see Fig. 13), a sizable temperature dependence is apparent in these spectra. With decreasing temperature, the optical SW is transferred from higher energies to the low-energy band around 1.9 eV. This temperature effect, measured on the aged surface of our $YTiO_3$ single crystal, is very similar to the observations recently reported by Gössling et al. [44]. However, one can hardly ascribe this temperature effect to spin-spin correlations, because the temperature changes are observable over a wide temperature range from 300 K to 15 K, and the high-temperature changes are much more pronounced than those that might be associated with the onset of correlated spin fluctuations at low temperatures. In addition, Fig. 7 shows that the optical conductivity spectra that exhibit a noticeable high-temperature effect, differ from those of measured on freshly polished surfaces. As discussed in Section III.C, we associate this phenomenon with the presence of defects of the titanium oxides, with the valency of Ti increased above 3^+, and nearby extra oxygen (interstitials) in the near-surface layer. The observed redistribution of the SW may then be associated with localized states at the edge of the p and d electronic bands.

IV. CONCLUSION

The detailed ellipsometric study presented here shows that oxygen defects can strongly modify the optical response in the near-surface region probed by the light beam. Extreme care must therefore be taken to maintain oxygen stoichiometry at the surface under investigation. The intrinsic optical response of $YTiO_3$ is broad, weakly anisotropic, and weakly temperature dependent. Nonetheless, using a careful study of the temperature dependence in combination with a dispersion analysis, we were able to identify an optical band at 2.9 eV whose energy, absolute spectral weight, and temperature dependence is consistent with the intersite $d_i^1 d_j^1 \longrightarrow d_i^2 d_j^0$ HS-state ($^3T_1$) optical transition. This indicates that $d-d$ transitions constitute a significant part of the optical response below the onset of dipole-allowed transitions be-

tween oxygen p- and titanium d-states at about 5 eV. However, this analysis accounts for only part of the optical response of $YTiO_3$. In particular, the origin of an intense optical band around 2 eV remains unclear. This indicates that other mechanisms, such as weakly dipole-allowed $p-d$ transitions or spin-polaron (or exciton-polaron) excitations, can contribute here significantly to the optical spectra. A more elaborate approach is required to obtain a quantitative description and verify the assignment of this optical band.

Our experiments also uncovered an important *qualitative* difference between $LaMnO_3$ and $YTiO_3$. In $LaMnO_3$, the spectral weight of inter-site $d-d$ transitions exhibits a strong anomaly upon heating above the Nèel temperature, followed by a more gradual temperature dependence due to short-range spin correlations at higher temperature. In $YTiO_3$, the optical spectral weight evolves smoothly through the onset of magnetic long-range order, with no discernible anomaly at the Curie temperature $T_C = 30$ K. However, a distinct anomaly is observed at about 100 K, far above T_C but coincident with a deviation of the uniform magnetization from mean-field Curie-Weiss behavior. This observation appears inconsistent with models in which the orbital degeneracy is completely quenched by lattice distortions, as it is in $LaMnO_3$, and gives credence to models that allow for a temperature-dependent orbital rearrangement. Our data therefore underscore the role of $YTiO_3$ as an interesting model system for the complex interplay between spin, orbital, and lattice degrees of freedom.

[1] M. Mochizuki and M. Imada, New Journal of Physics **6**, 154 (2004); M. Mochizuki and M. Imada, J. Phys. Soc. Japan **69**, 1982 (2000); M. Mochizuki and M. Imada, J. Phys. Soc. Japan **70**, 1777 (2001).

[2] E. Pavarini, S. Biermann, A. Poteryaev, A. I. Lichtenstein, A. Georges, and O.K. Andersen, Phys. Rev. Lett. **92**, 176403 (2004); E. Pavarini, A. Yamasaki, J. Nuss, and O.K. Andersen, New J. Phys. **7**, 188 (2005) (http://www.njp.org).

[3] R. Schmitz, O. Entin–Wohlman, A. Aharony, A. B. Harris, and E. Müller-Hartmann, Phys. Rev. B **71**, 144412 (2005).

[4] I. V. Solovyev, Phys. Rev. B **74**, 054412 (2006).

[5] T. Mizokawa, D. I. Khomskii, and G. A. Sawatzky, Phys. Rev. B **60**, 7309 (1999).

[6] J. Akimitsu, H. Ichikawa, N. Eguchi, T. Miyano, M. Nishi, and K. Kakurai, J. Phys. Soc. Jpn. **70**, 3475 (2001).

[7] M.W. Haverkort, Z. Hu, A. Tanaka, G. Ghiringhelli, H. Roth, M. Cwik, T. Lorenz, C. Schüssler–Langeheine, S.V. Streltsov, A.S. Mylnikova, V.I. Anisimov, C. de Nadai, N.B. Brookes, H.H. Hsieh, H.-J. Lin, C.T. Chen, T. Mizokawa, Y. Taguchi, Y. Tokura, D.I. Khomskii, and L. H. Tjeng, Phys. Rev. Lett. **94**, 056401 (2005).

[8] M. Itoh, M. Tsuchiya, H. Tanaka, and K. Motoya, J. Phys. Soc. Jpn. **68**, 2783 (1999).

[9] C. Ulrich, G. Khaliullin, S. Okamoto, M. Reehuis, A. Ivanov, H. He, Y. Taguchi, Y. Tokura, and B. Keimer, Phys. Rev. Lett. **89**, 167202 (2002).

[10] C. Ulrich, A. Gössling, M. Grüninger, M. Guennou, H. Roth, M. Cwik, T. Lorenz, G. Khaliullin, and B. Keimer, Phys. Rev. Lett. **97**, 157401 (2006).

[11] G. Khaliullin and S. Okamoto, Phys. Rev. Lett. **89**, 167201 (2002); G. Khaliullin and S. Okamoto, Phys. Rev. B **68**, 205109 (2003); G. Khaliullin, Prog. Theor. Phys. **60**, 155 (2005).

[12] N. N. Kovaleva, A. V. Boris, C. Bernhard, A. Kulakov, A. Pimenov, A. M. Balbashov, G. Khaliullin, and B. Keimer, Phys. Rev. Lett. **93**, 147204 (2004).

[13] K. Tobe, T. Kimura, Y. Okimoto, and Y. Tokura, Phys. Rev. B **64**, 184421 (2001).

[14] M. Cwik, T. Lorenz, J. Baier, R. Müller, G. André, F. Bourée, F. Lichtenberg, A. Freimuth, R. Schmitz, E. Müller–Hartmann, and M. Braden, Phys. Rev. B **68**, 060401(R) (2003).

[15] D. A. Maclean, Hok-Nam NG, and J. E. Greedan, J. Solid State Chem. **30**, 35 (1979).

[16] M. Tsubota, F. Iga, T. Takabatake, N. Kikugawa, T. Suzuki, I. Oguro, H. Kawanaka, H. Bando, Physica B **281-282**, 622 (2000).

[17] J. D. Garret, J. E. Greedan, D. A. MacLean, Mater. Res. Bull. **16**, 145 (1981).

[18] J. Kircher, J. Humliček, M. Garriga, M. Cardona, D. Fuchs, H.-U. Habermeier, O. Jepsen, Sudha Gopalan, O. K. Andersen, Y. Fang, U. Welp, K. G. Vandervoort, and G. W. Crabtree, Physica C **192**, 473 (1992).

[19] C. Bernhard, J. Humliček, and B. Keimer, Thin Solid Films **455-456**, 143 (2004).

[20] Y. Okimoto, T. Katsufuji, Y. Okada, T. Arima, and Y. Tokura, Phys. Rev. B **51**, 9581 (1995).

[21] Y. Taguchi, Y. Tokura, T. Arima, and F. Inaba, Phys. Rev. B **48**, 511 (1993).

[22] C. Noguera, J. Phys.: Condens. Matter **12**, R367 (2000).

[23] R. A. Evarestov, E. A. Kotomin, D. Fuks, J. Felsteiner, and J. Maier, Appl. Surf. Sci. **238**, 457 (2004); R. A. Evarestov, E. A. Kotomin, Yu. A. Mastrikov, D. Gryaznov, E. Heifets, and J. Maier, Phys. Rev. B **72**, 214411 (2005).

[24] T. Arima and Y. Tokura, J. Phys. Soc. Japan **64**, 2488 (1995).

[25] T. Katsufuji, Y. Okimoto, and Y. Tokura, Phys. Rev. Lett. **75**, 3497 (1995).

[26] S. Bouarab, A. Vega, and M. A. Khan, Phys. Rev. B **54**, 11271 (1996).

[27] O. V. Krasovska, V. N. Antonov, E. E. Krasovskii, and W. Schattke, Phys. stat. sol.(b) **243**, 1885 (2006).

[28] I. Solovyev, N. Hamada, and K. Terakura, Phys. Rev. B **53**, 7158 (1996).

[29] A. V. Zenkov, Phys. stat. sol.(b) **241**, 2508 (2004).

[30] A. M. Oleś, G. Khaliullin, P. Horsch, and L. F. Feiner, Phys. Rev. B **72**, 214431 (2005).

[31] V. Fritsch, J. Hemberger, M. V. Eremin, H.-A. Krug von Nidda, F. Lichtenberg, R. Wehn, and A. Loidl, Phys. Rev. B **65**, 212405 (2002).

[32] T. Higuchi, D. Baba, T. Takeuchi, T. Tsukamoto, Y. Taguchi, Y. Tokura, A. Chainani, S. Shin, Phys. Rev. B **68**, 104420-1 (2003).

[33] J. S. Griffith, *The Theory of Transition-Metal Ions*, (Cambridge University Press, Cambridge, England, 1961).

[34] D. van der Marel, G. A. Sawatzky, Phys. Rev. B **37**, 10674 (1988).

[35] T. Mizokawa and A. Fujimori, Phys. Rev. B **54**, 5368 (1996).

[36] A. E. Bocquet, T. Mizokawa, K. Morikawa, and A. Fujimori, S. R. Barman, K. Maiti, D. D. Sarma, Y. Tokura, and M. Onoda, Phys. Rev. B **53**, 1161 (1996).

[37] F. Aryasetiawan, K. Karlsson, O. Jepsen, and U. Schönberger, Phys. Rev. B, **74**, 125106 (2006).

[38] A. M. Stoneham and M. J. L. Sangster, Phil. Mag. **B43**, 609 (1980).

[39] N. N. Kovaleva, J. L. Gavartin, A. L. Shluger, A. V. Boris, and A. M. Stoneham, JETP **94**, 178 (2002).

[40] S. Aljishi, J. D. Cohen, Shu Jin, and L. Ley, Phys. Rev. Lett. **64**, 2811 (1990).

[41] U. Öpik, M. H. Pryce, Proc. R. Soc. A**238**, 425 (1957).

[42] A. M. Stoneham, *Theory of Defects in Solids*, (Clarendon Press, Oxford, 1975).

[43] G. Khaliullin, P. Horsch, and A. M. Oleś, Phys. Rev. B **70**, 195103 (2004).

[44] A. Gössling, R. Schmitz, H. Roth, M.W. Haverkort, T. Lorenz, J.A. Mydosh, E. Müller-Hartmann, M. Grüninger, cond-mat/0608531 24 Aug 2006.
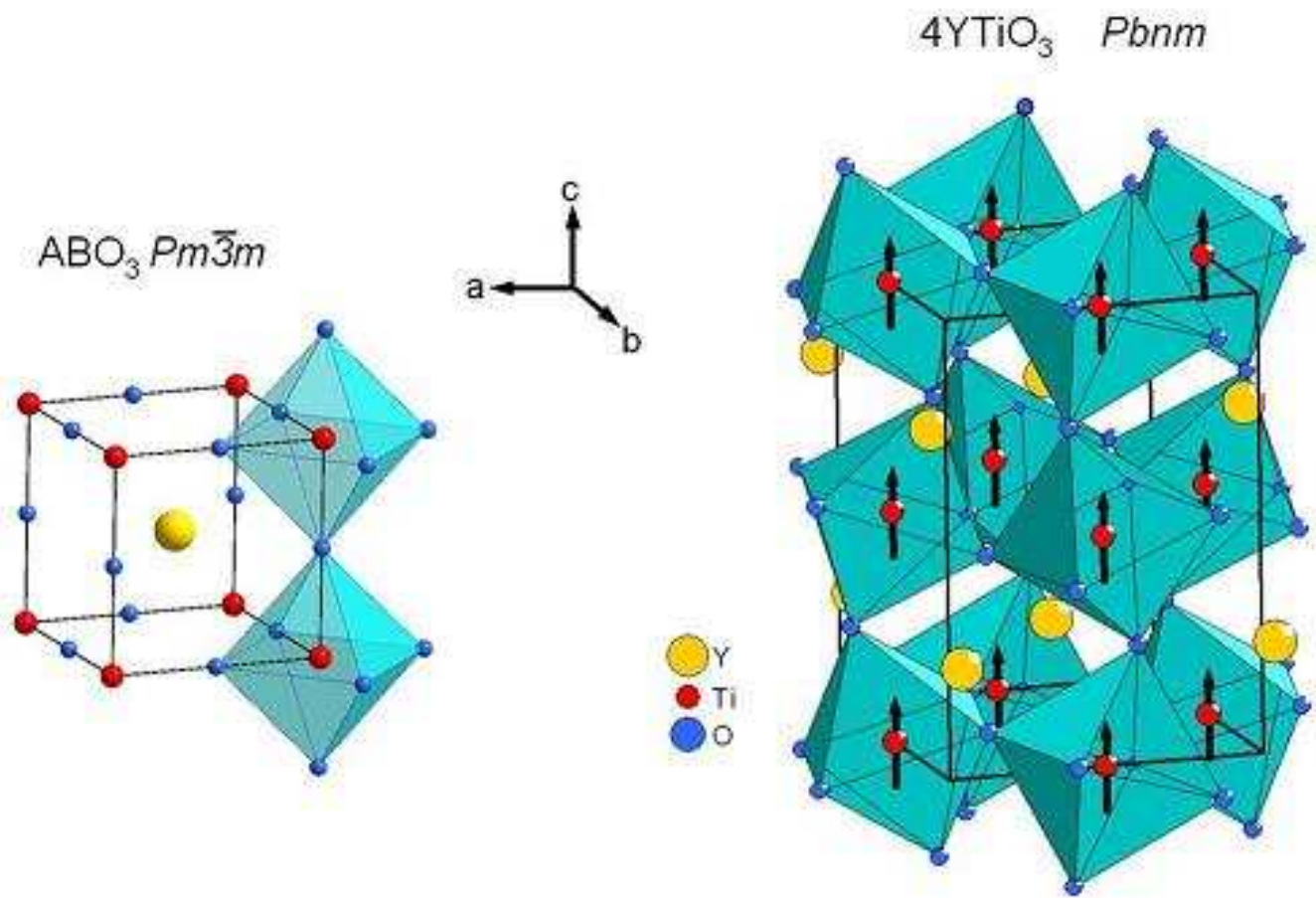
.

ABO$_3$ $Pm\overline{3}m$

4YTiO$_3$ $Pbnm$

O Y
● Ti
O O

FIG. 1: (Color) Crystal structures of cubic perovskite oxides of the formula ABO$_3$ (space group $Pm\overline{3}m$), where A is a rare-earth atom (yellow sphere) and B is a transition-metal atom (red spheres) (left), and related orthorhombic structure of YTiO$_3$ (space group $Pbnm$) with GdFeO$_3$-type distortions, with ferromagnetic alignment of Ti spins shown schematically (right).
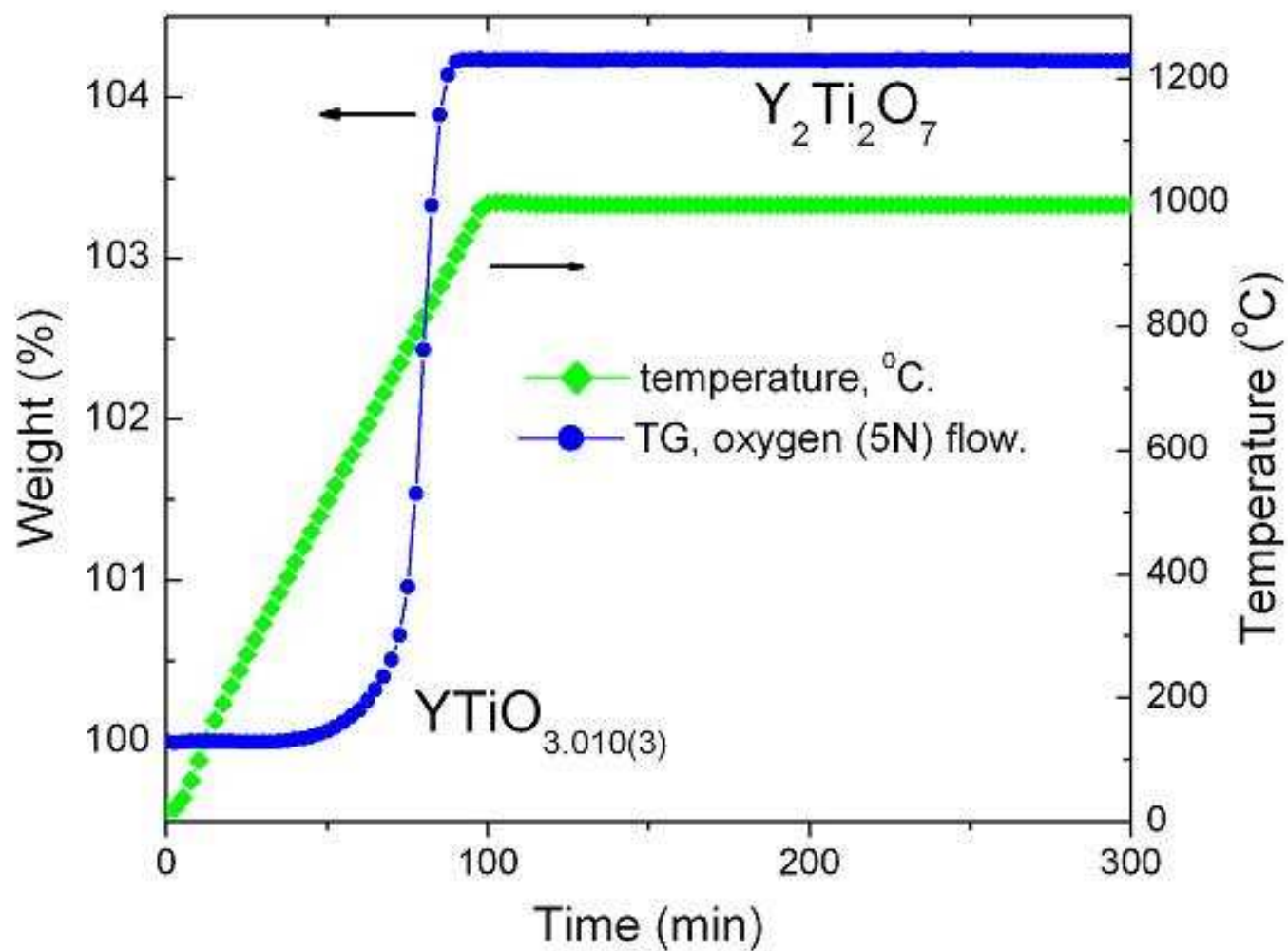
FIG. 2: (Color online) Weight gain (circles) of $YTiO_3$ sample in oxygen atmosphere versus temperature (squares). As a result of full oxidation of Ti^{3+} to Ti^{4+} $Y_2Ti_2O_7$ compound is stabilized.
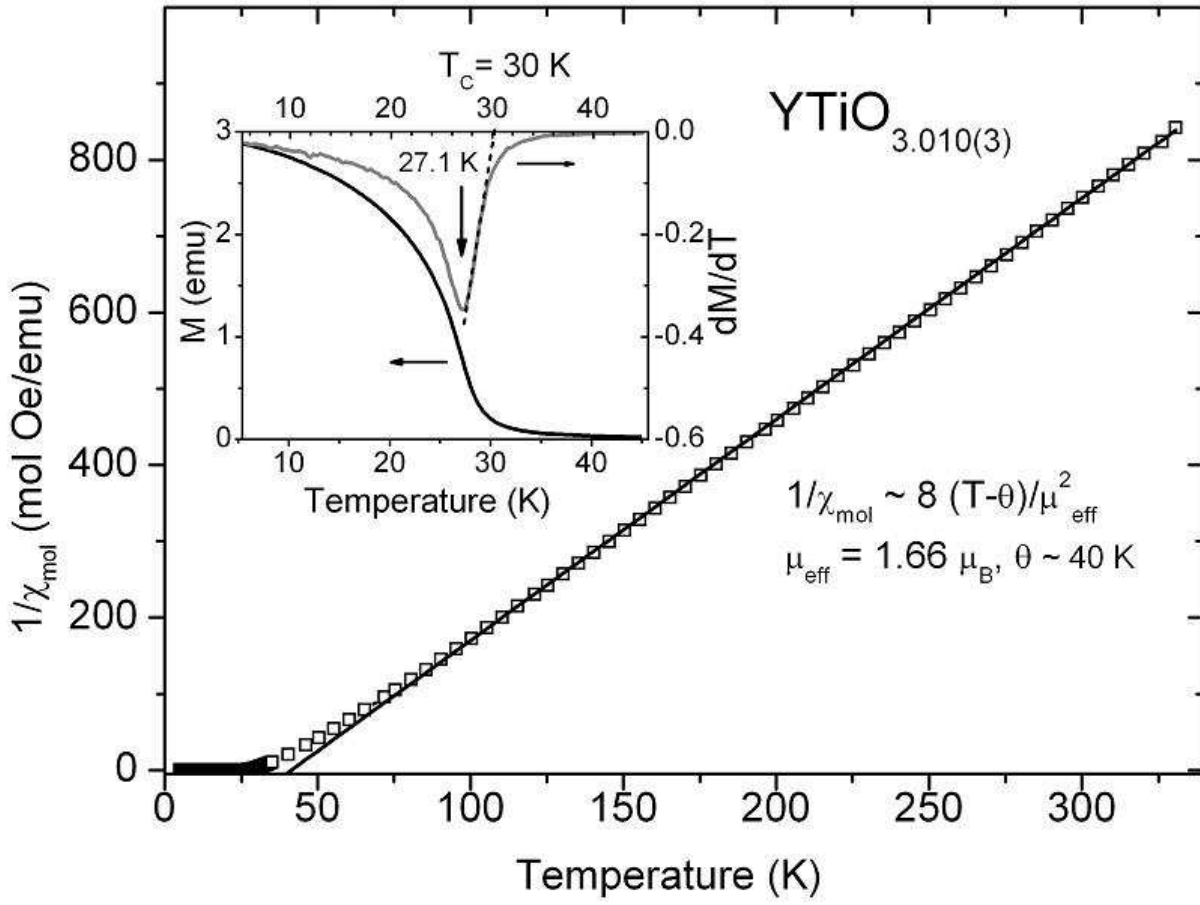
FIG. 3: Temperature dependence of inverse susceptibility (squares) of YTiO$_3$ single crystal approximated by Curie-Weiss behavior at high temperatures (solid line). The inset shows temperature dependence of magnetization in the vicinity of T$_C$ and its temperature derivative after zero-field cooling in magnetic field of 1000 Oe with **H** ∥ c. An inflection point in temperature-dependent magnetization is observed at 27 K.
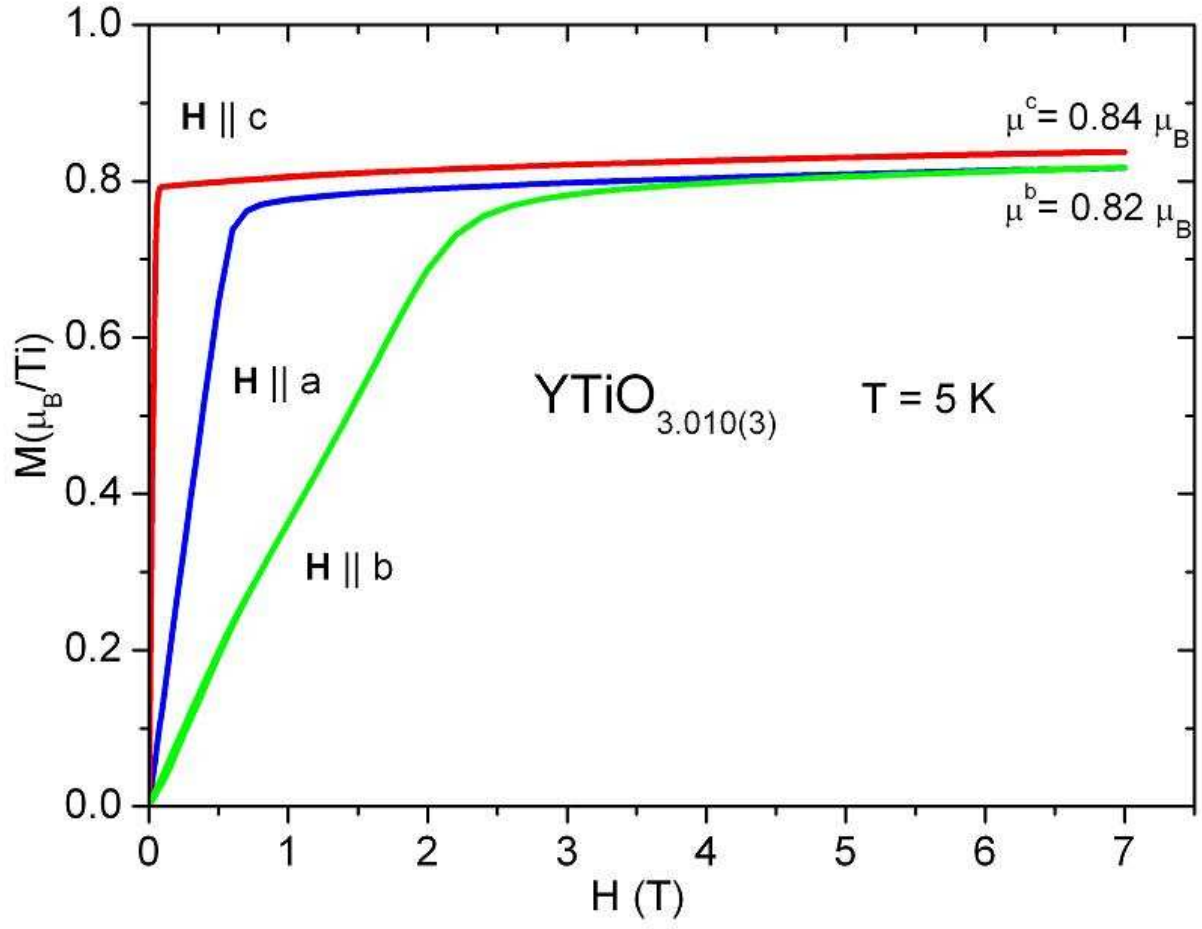
FIG. 4: (Color online) Magnetization of YTiO$_3$ single crystal measured with magnetic field applied along a-, b-, and c-axes (in *Pbnm* notation) at T = 5 K.
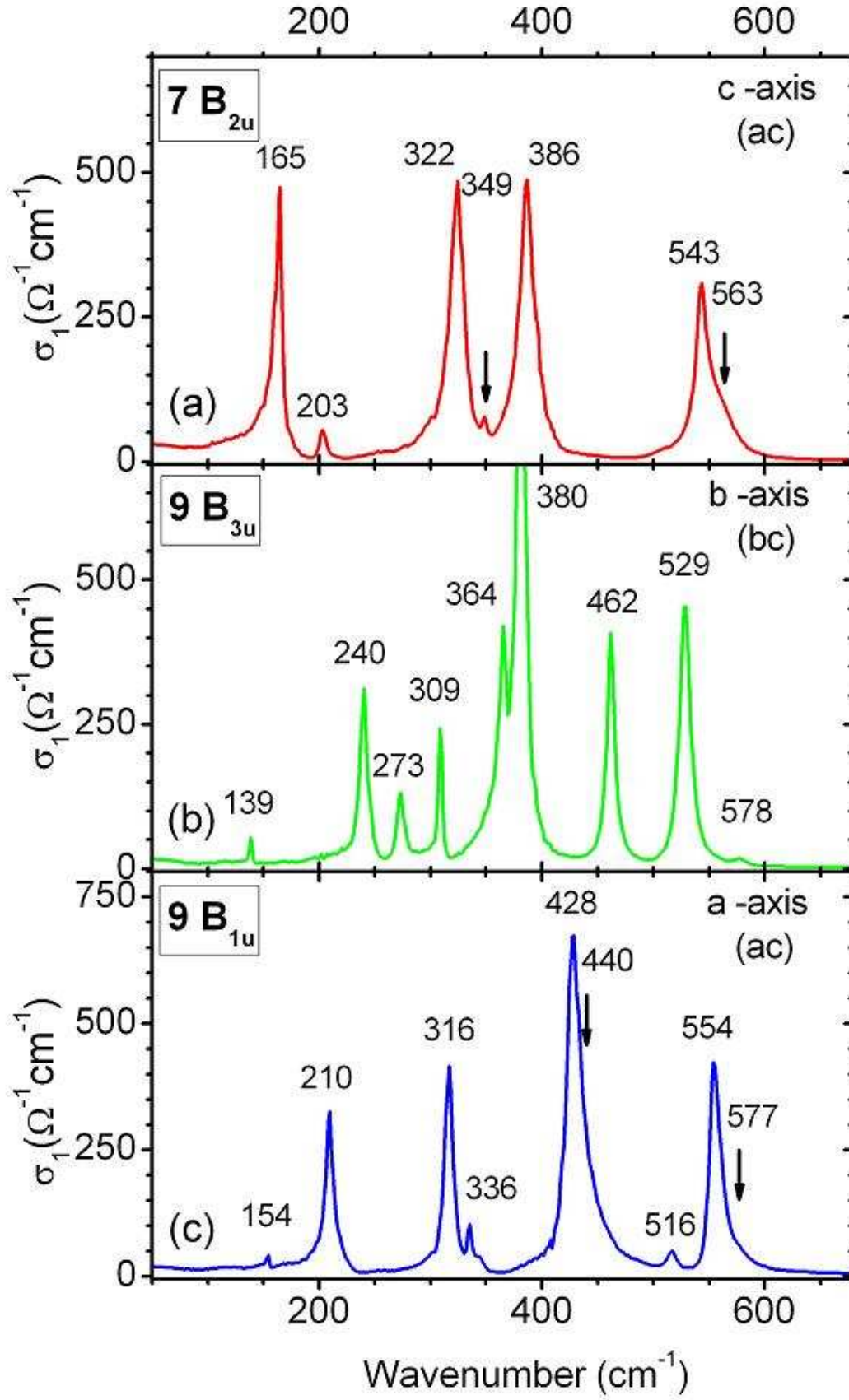
FIG. 5: (Color online) IR-active optical phonons from polarized reflectivity measurements along (a) *c*-axis, (b) *b*-axis, and (c) *a*-axis at T = 15 K.
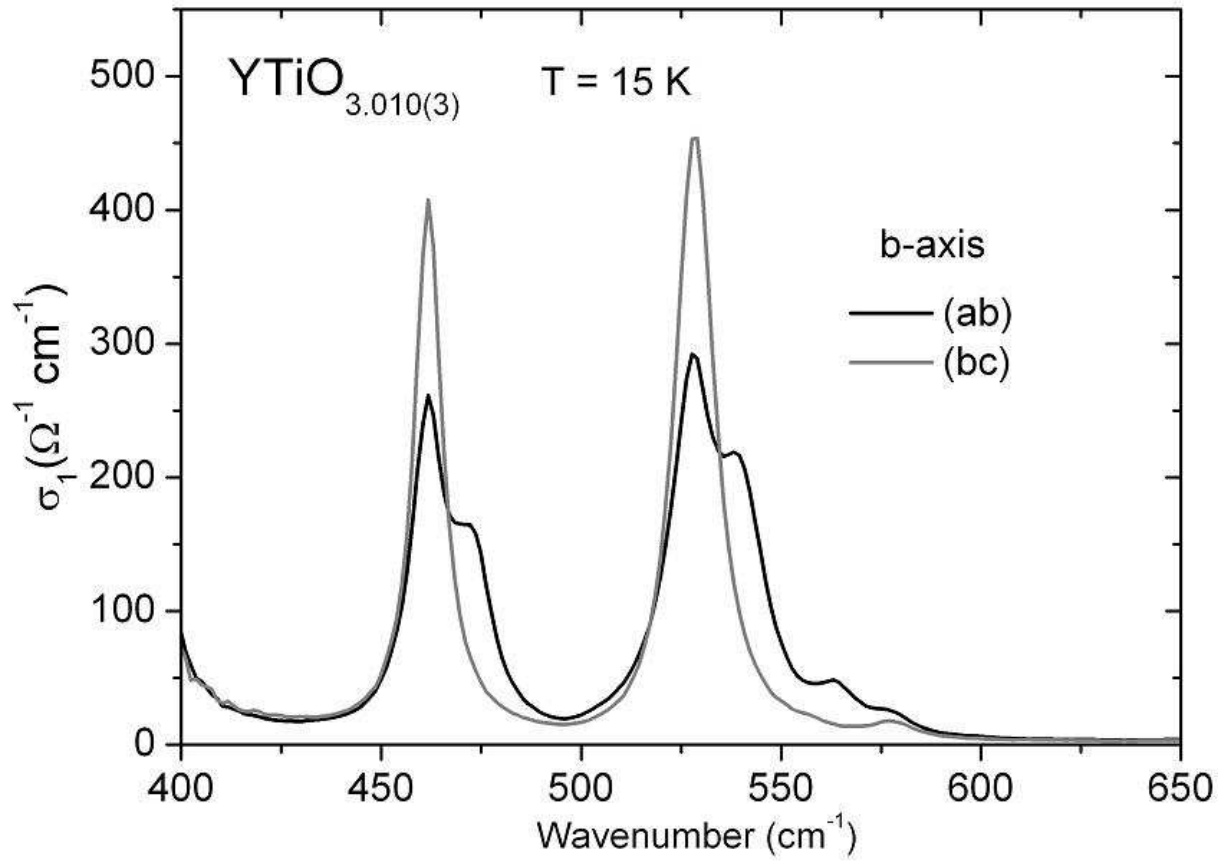
FIG. 6: Oxygen-dominated b-axis optical phonons in $YTiO_3$ single crystal measured on ab and bc surfaces at 15 K.
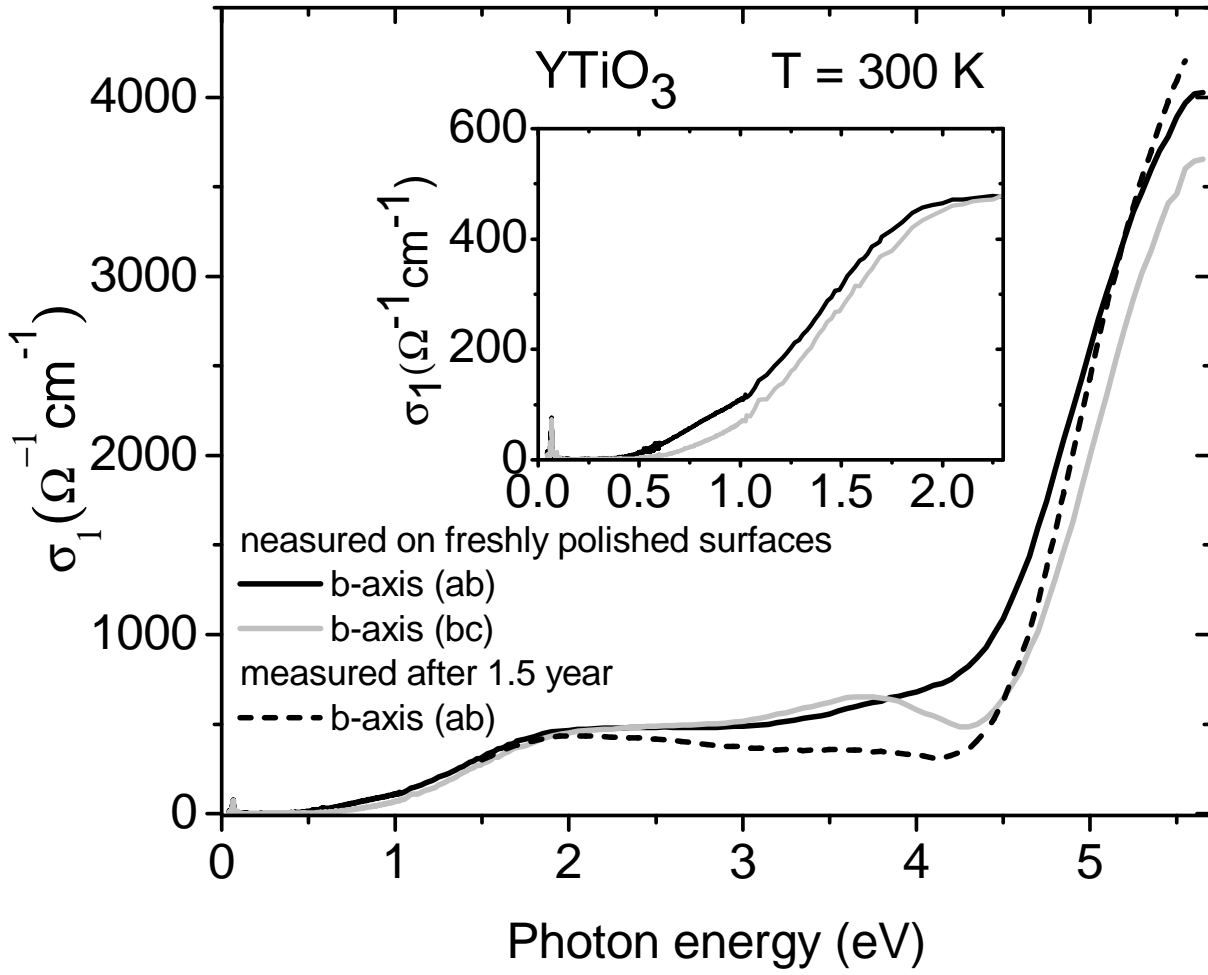
FIG. 7: *B*-axis optical conductivity spectra measured on freshly polished *ab* and *bc* surfaces and on aged *ab* surface at T = 300 K. The inset shows details near the absorption edge.
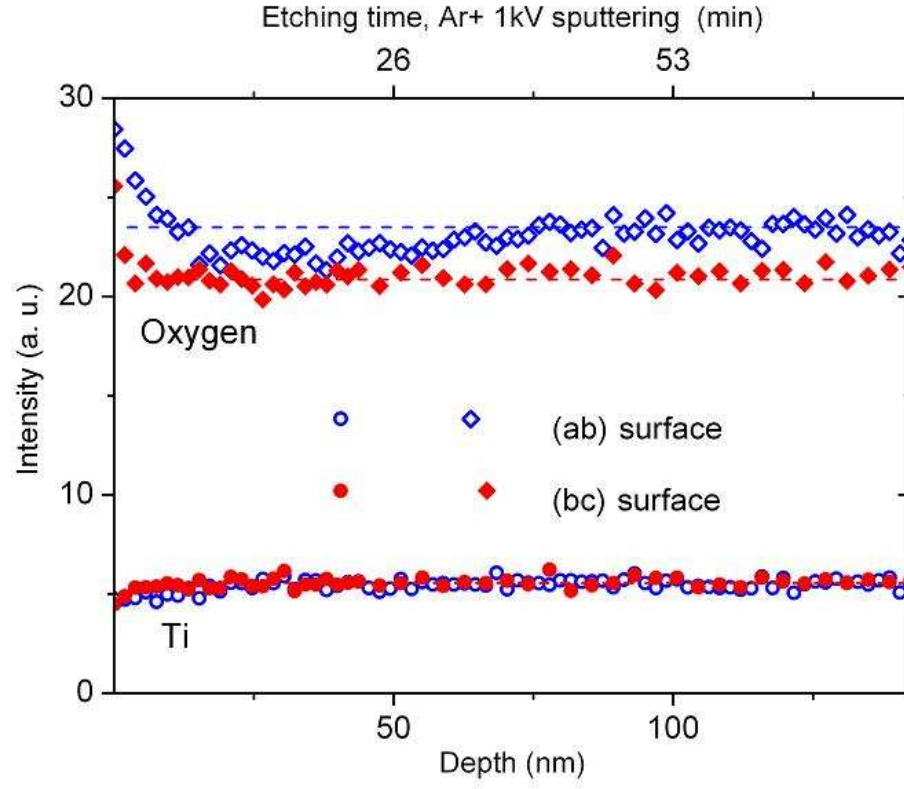
FIG. 8: (Color online) AES sputter-depth profiles on the *ab* and *bc* surfaces in orthorhombic YTiO₃ (*Pbnm*), associated with (001)- and (110)-perovskite-type surfaces.
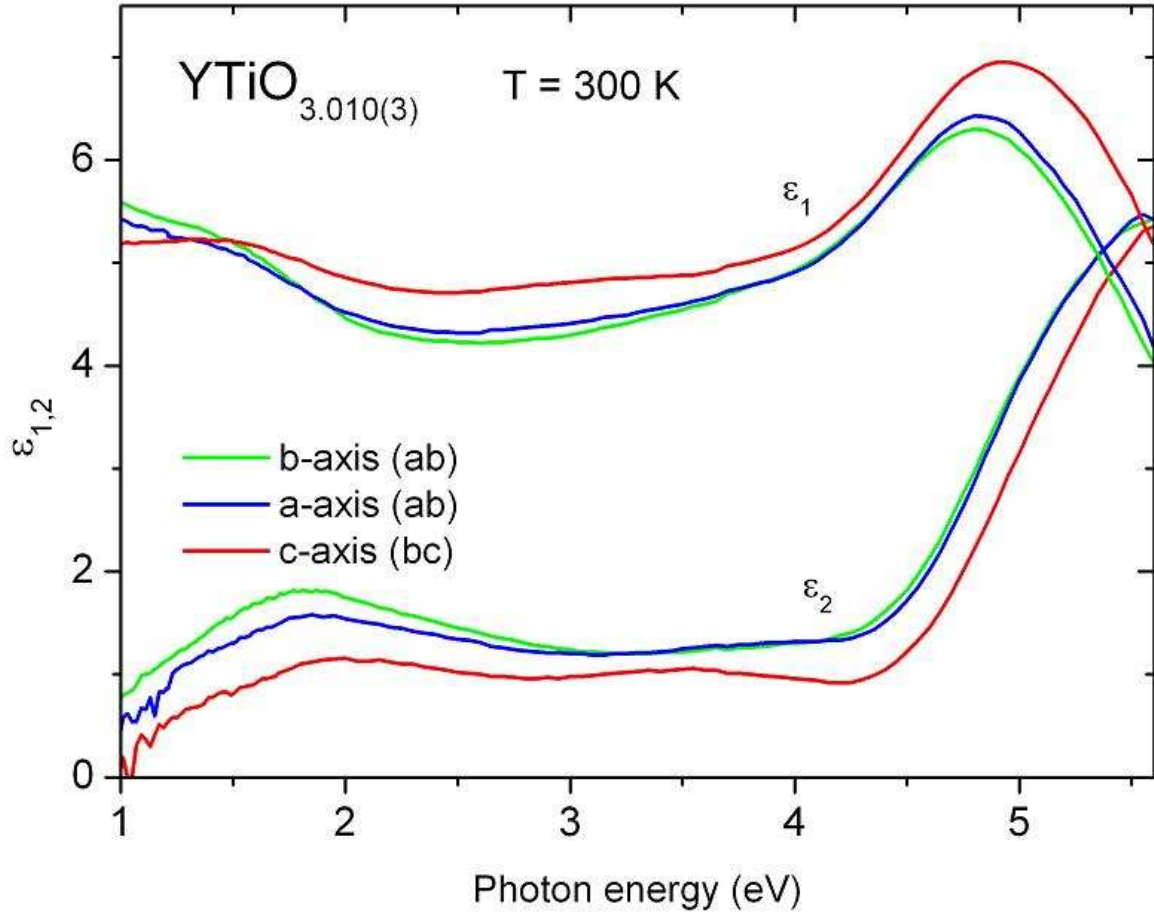
FIG. 9: (Color) Dielectric function of YTiO$_3$ single crystal in a- and b-axis polarizations measured on ab plane, and in c-axis polarization measured on bc plane at T = 300 K.
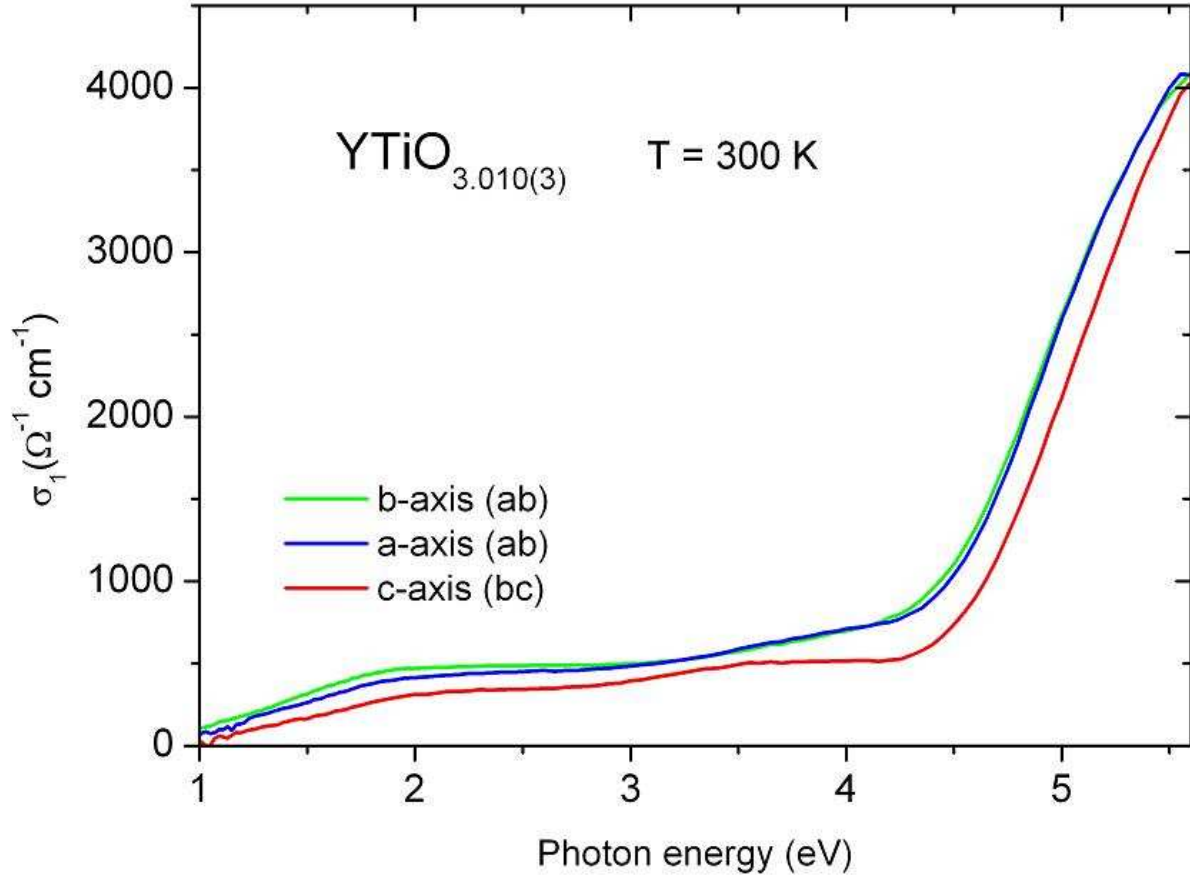
FIG. 10: (Color) Optical conductivity of YTiO$_3$ single crystal in a- and b-axis polarizations measured on ab plane, and in c-axis polarization measured on bc plane at T = 300 K.
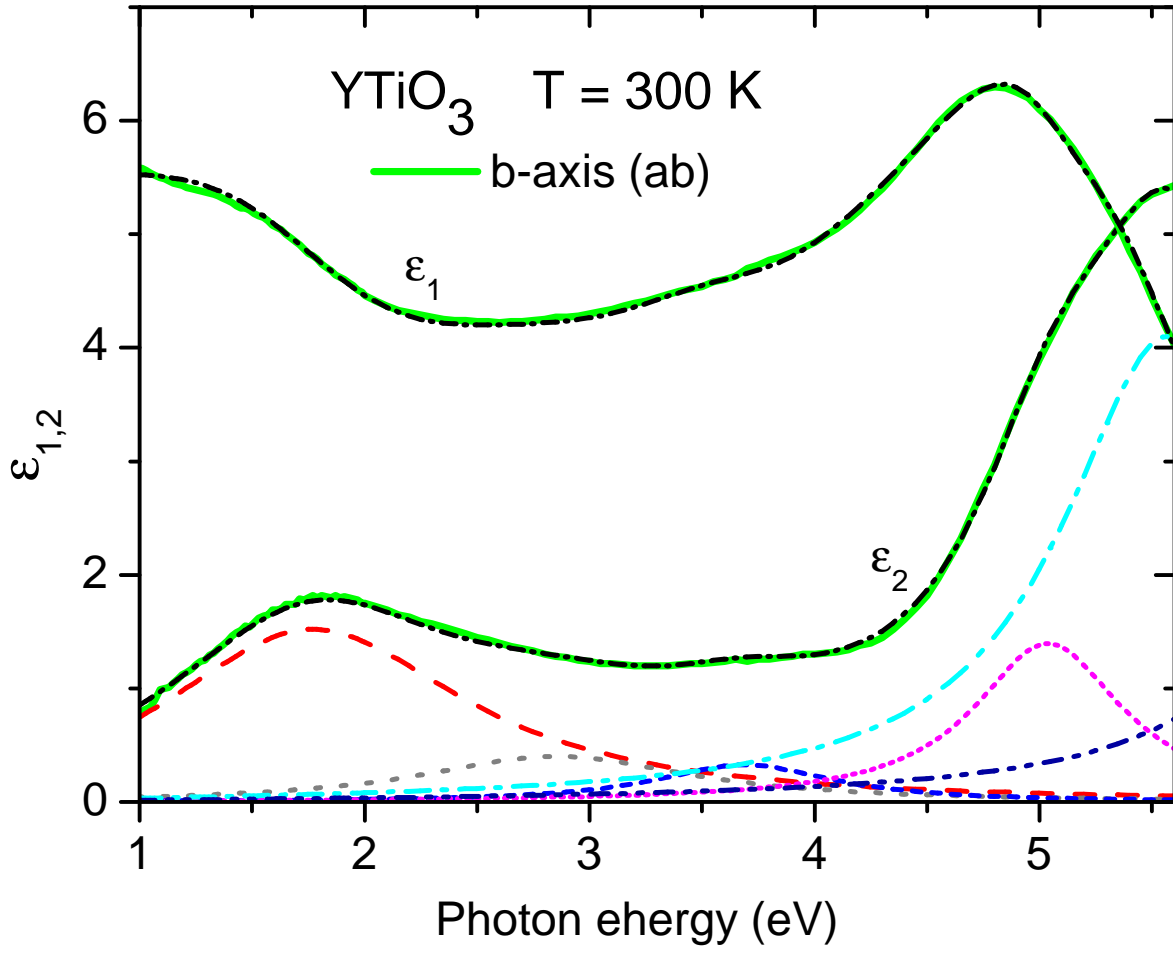
FIG. 11: (Color online) B-axis dielectric response $\tilde{\epsilon}(\nu)$ at 300 K, represented by total contribution (black dash-dotted curves) of separate Lorentzian bands determined by the dispersion analysis, as described in the text. Peak energies ν_j, widths γ_j, and dimensionless oscillator strengths S_j, of Lorentzian bands are listed in Table 1.
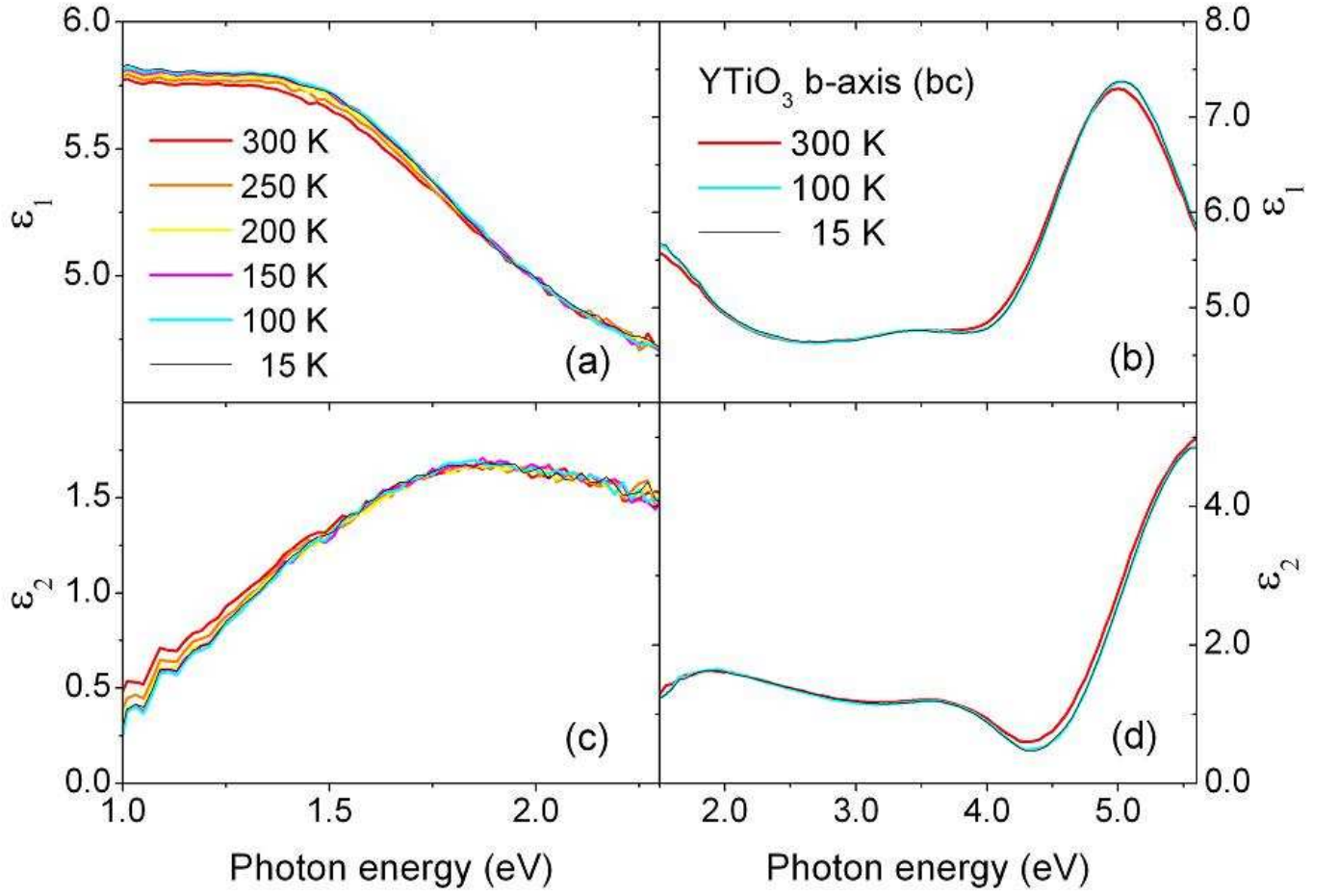
FIG. 12: (Color) Temperature dependences of: (a) and (b) $\epsilon_1(\nu)$ and (c) and (d) $\epsilon_2(\nu)$ of YTiO$_3$ single crystal measured in b-axis polarization on bc plane. Left panels detail changes of complex dielectric response near the absorption edge; right panels show its major changes at higher energies.
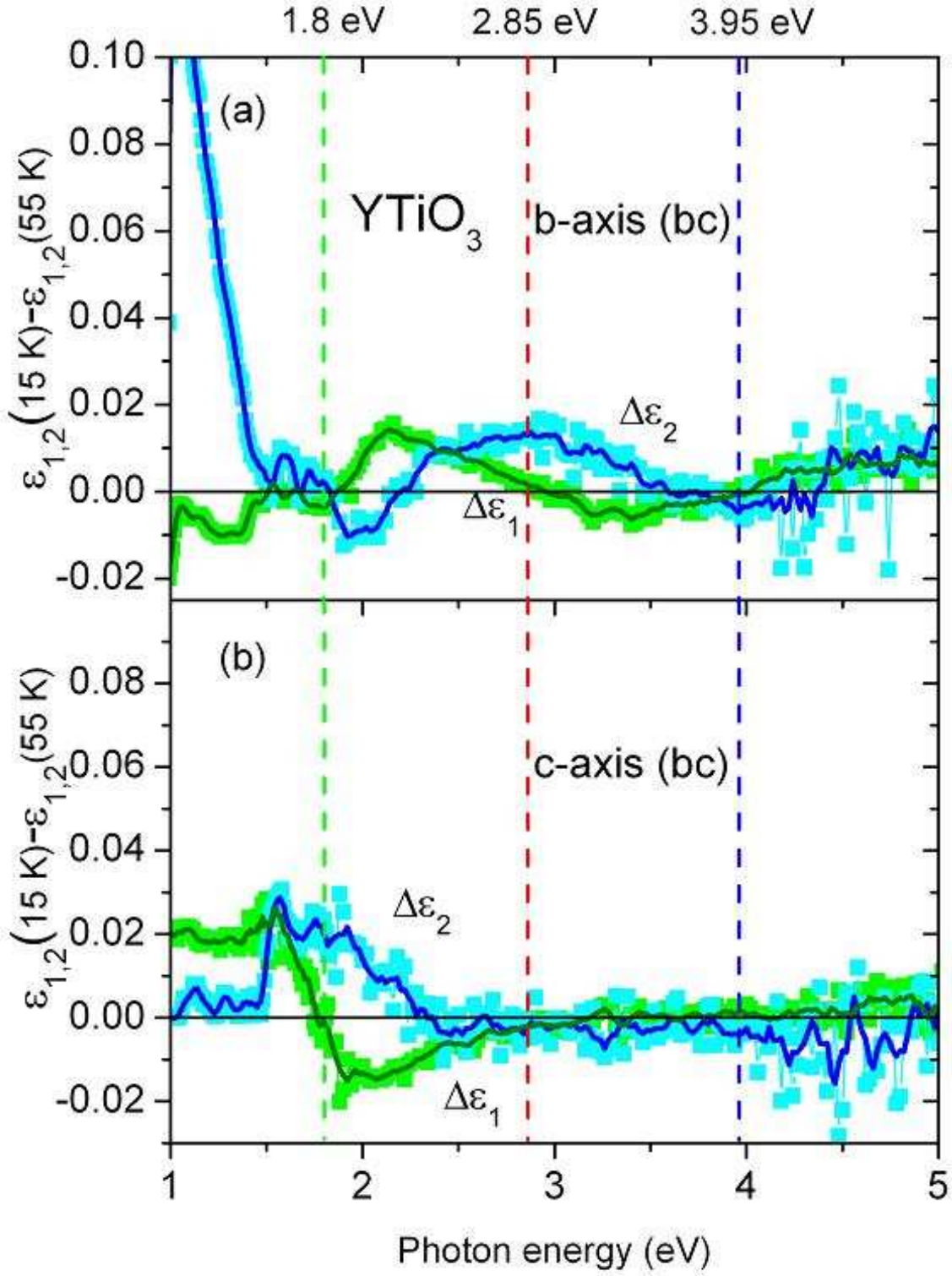
FIG. 13: (Color) Changes in b- and c-axis complex dielectric response $\tilde{\epsilon}(\nu)$ of YTiO$_3$ single crystal between 15 and 55 K (solid curves are result of averaging). Vertical lines mark photon energies at which resonant behavior in $\Delta\epsilon_2(\nu)$ coincides with zero-crossing in $\Delta\epsilon_1(\nu)$ in b- and/or c-axis polarization(s).
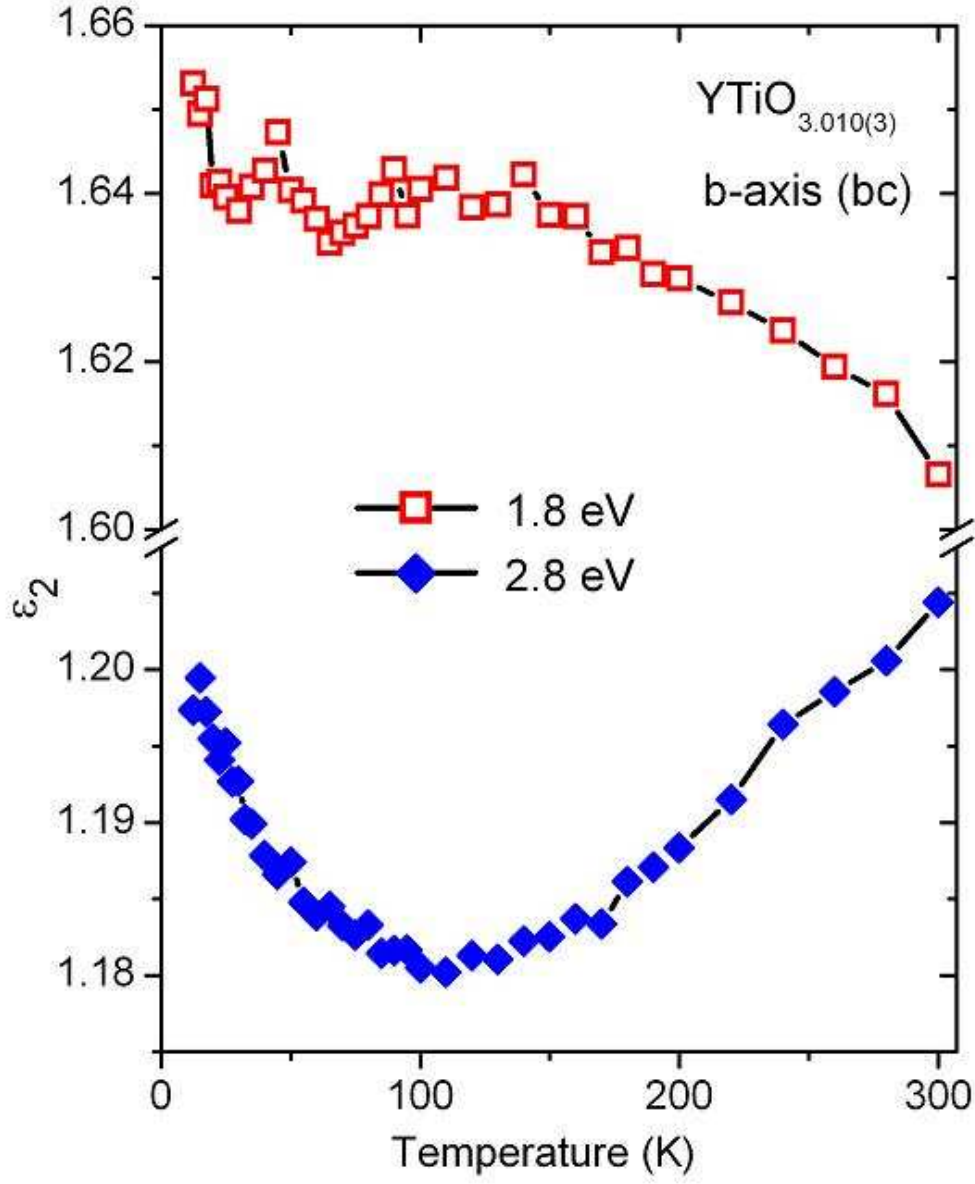
FIG. 14: (Color online) Temperature dependences of ϵ_2 intensities at the peak positions 1.8 and 2.85 eV in b-axis polarization.
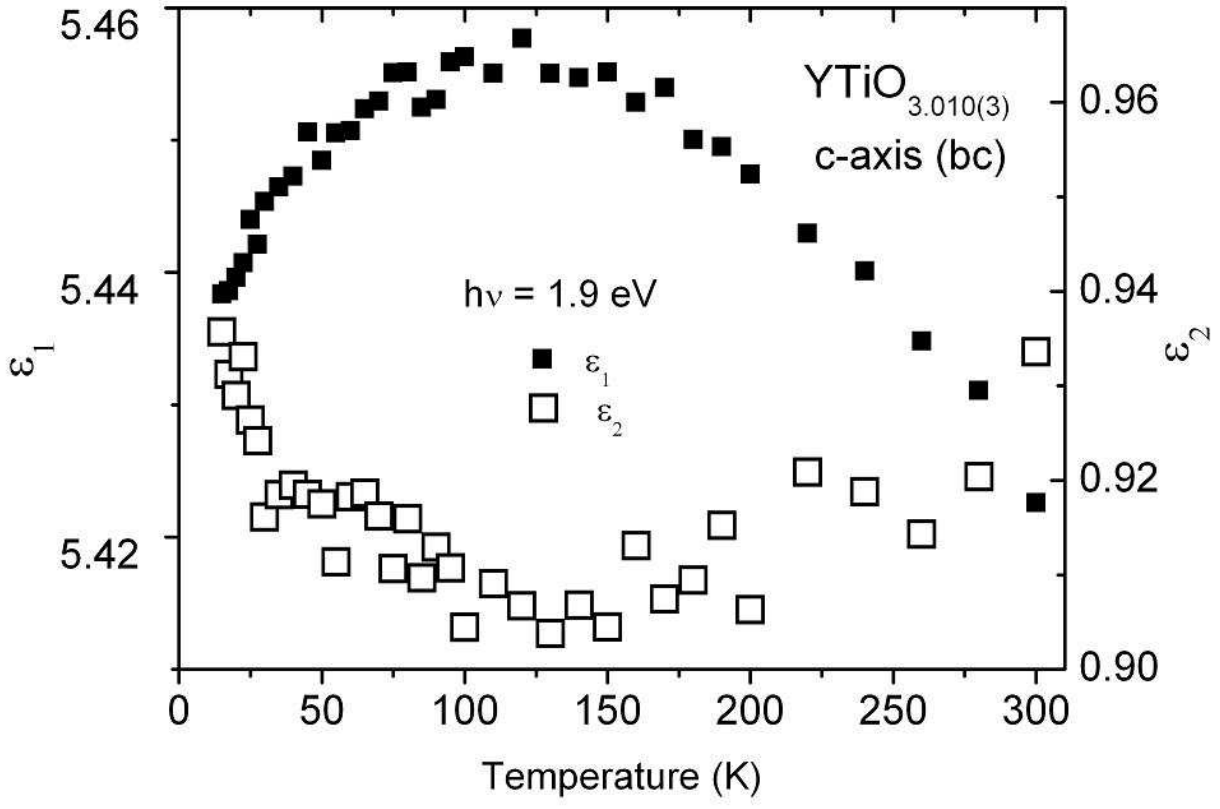
FIG. 15: Temperature dependences of ϵ_1 and ϵ_2 intensities slightly off-resonance to the peak position at 1.8 eV in c-axis polarization.
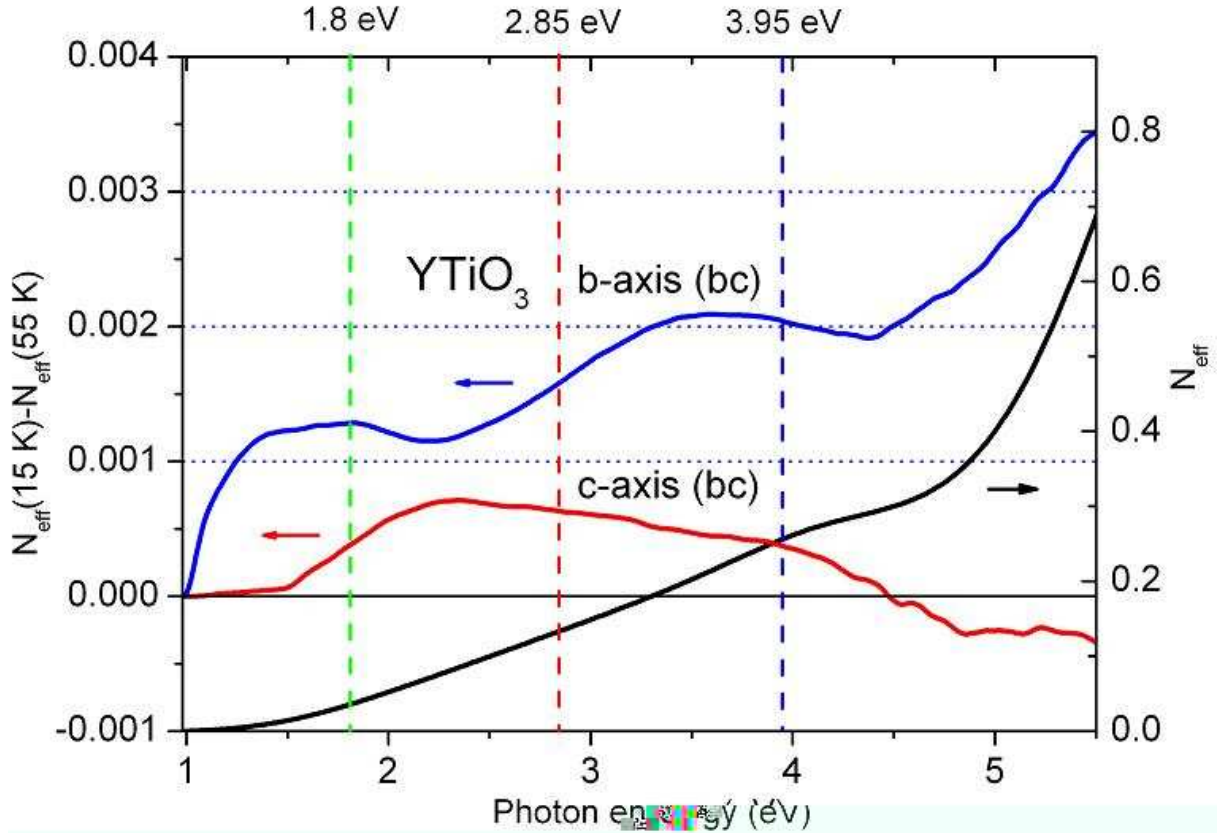
FIG. 16: (Color online) Spectral weight changes $\Delta N_{eff}(\nu)$ between 15 and 55 K in b- and c-axis polarizations of $YTiO_3$ single crystal and b-axis $N_{eff}(\nu)$ spectrum at 15 K. Vertical lines mark peak positions of temperature-dependent optical bands in b- and/or c-axis polarization(s).
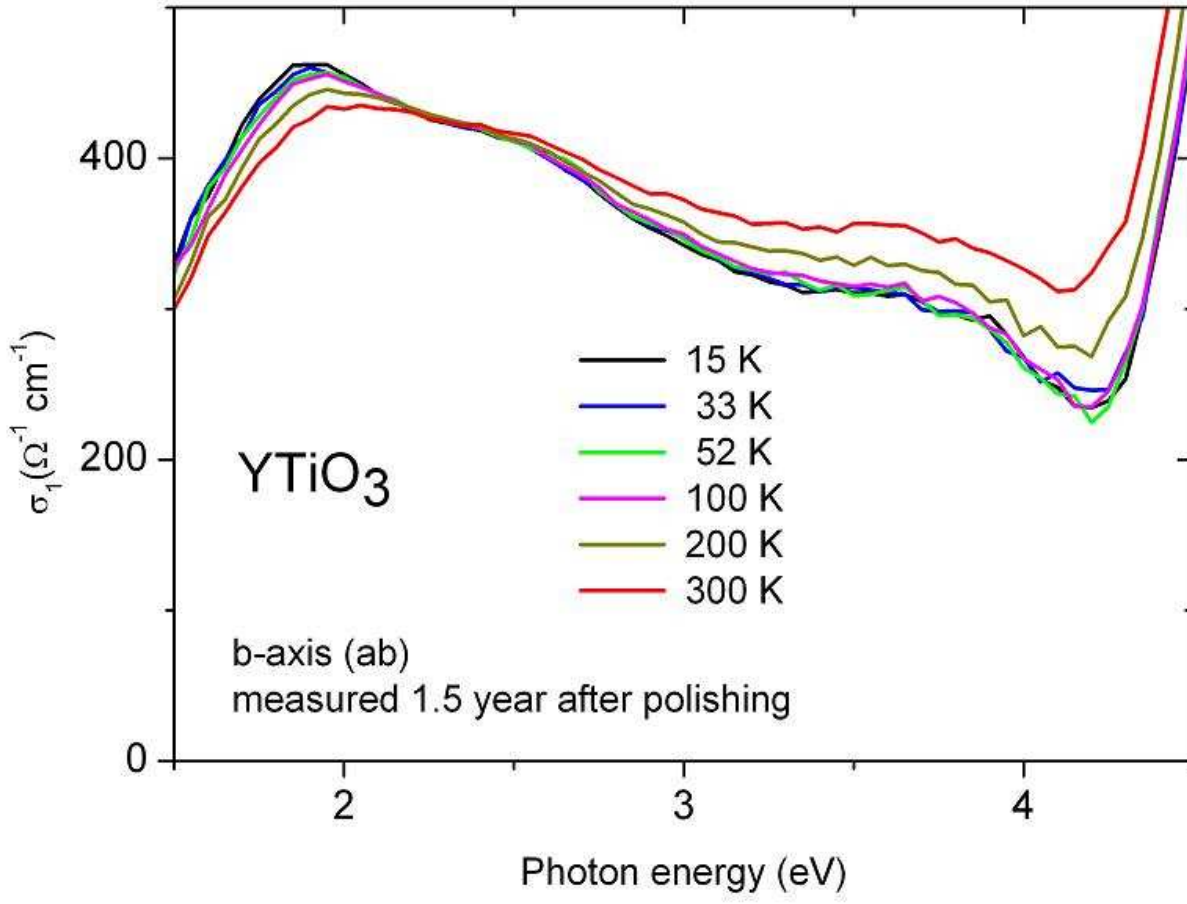
FIG. 17: (Color) $\sigma_1(T)$ measured on the aged surface of YTiO$_3$ single crystal.